Check for updates

JGR Solid Earth

RESEARCH ARTICLE
10.1029/2023JB026506

Broadband Strong Ground Motion Modeling Using Planar Dynamic Rupture With Fractal Parameters

F. Gallovič[1] and Ľ. Valentová[1]

[1]Faculty of Mathematics and Physics, Charles University, Prague, Czech Republic

Key Points:

- We propose a robust procedure to enrich a smooth dynamic source model by random fractal small-scale perturbations
- The resulting rupture acceleration and deceleration enhance high-frequency radiation, improving fit to observed broadband ground motions
- The approach effectively introduces small-scale complexities to planar faults, permitting applications in seismic hazard assessment

Supporting Information:

Supporting Information may be found in the online version of this article.

Correspondence to:

F. Gallovič,
frantisek.gallovic@matfyz.cuni.cz

Citation:

Gallovič, F., & Valentová, Ľ. (2023). Broadband strong ground motion modeling using planar dynamic rupture with fractal parameters. *Journal of Geophysical Research: Solid Earth*, *128*, e2023JB026506. https://doi.org/10.1029/2023JB026506

Received 3 FEB 2023
Accepted 12 MAY 2023

Author Contributions:

Conceptualization: F. Gallovič
Data curation: F. Gallovič
Formal analysis: F. Gallovič, Ľ. Valentová
Funding acquisition: F. Gallovič
Investigation: F. Gallovič, Ľ. Valentová
Methodology: F. Gallovič
Project Administration: F. Gallovič
Resources: F. Gallovič
Software: F. Gallovič, Ľ. Valentová
Supervision: F. Gallovič
Validation: F. Gallovič, Ľ. Valentová
Visualization: F. Gallovič, Ľ. Valentová

© 2023 The Authors.
This is an open access article under the terms of the Creative Commons Attribution-NonCommercial License, which permits use, distribution and reproduction in any medium, provided the original work is properly cited and is not used for commercial purposes.

Abstract Dynamic rupture modeling represents a promising physics-based approach to strong ground motion simulations. However, its application in a broad frequency range (0–10 Hz), interesting for engineering studies, is challenging. The main reason is that widely used and relatively simple planar fault models with smooth distributions of initial stress and frictional parameters, or even self-similar initial stress, result in ground motions depleted in high-frequency content. Here we propose an efficient approach for the linear slip-weakening friction model on a planar fault based on the Ide and Aochi (2005, https://doi.org/10.1029/2004jb003591) multiscale model with a small-scale random fractal distribution of the slip-weakening distance D_c. We propose a way to combine these variations with a large-scale deterministic dynamic model. We illustrate the approach on an elliptical model and a smooth model of the 2016 M_w 6.2 Amatrice, Italy, earthquake from low-frequency dynamic rupture inversion. To intensify the incoherence of the rupture propagation, we also include a variation of the strength and initial stress, both correlated with D_c. These additions result in sustained high-frequency radiation during the whole rupture propagation and omega-square source time functions. The new model of the Amatrice earthquake generates synthetics that agree with the local ground motion model up to 5 Hz in terms of spectral accelerations while preserving the average and integral dynamic rupture parameters (e.g., stress drop, fracture and radiated energy). The fractal dynamic model can be easily implemented in any dynamic rupture propagation code and is thus readily applicable in broadband physics-based ground motion predictions for earthquake scenarios in seismic hazard assessment.

Plain Language Summary Earthquake dynamic rupture models are usually simple and smooth because they are retrieved from low-frequency data to avoid high-frequency content that cannot be modeled deterministically. These models then underestimate observed ground motions at frequencies above 1 Hz, which are important in engineering applications. Adding small-scale complexities such as rough fault geometry to refine the models is numerically demanding, requiring supercomputers, and thus preventing their widespread use. Here we propose a relatively simple approach to add suitable small-scale variations applicable to planar fault models, permitting very efficient computer calculations. An initially smooth dynamic model is enriched by random fractal perturbations to preserve the large-scale rupture properties. The resulting small-scale acceleration and deceleration of the rupture enhance the source radiation at high frequencies throughout the rupture process. As an example, the approach is applied to the smooth 2016 M6.2 Amatrice earthquake model constrained by low-frequency data. We demonstrate that the fractal additions preserve the data-constrained large-scale characteristics of the model and improve its agreement with ground motions up to 10 Hz. The technique can be readily implemented in physics-based earthquake rupture modeling applicable in, for example, seismic hazard applications.

1. Introduction

Modeling of broadband strong ground motions is traditionally performed using kinematic methods that prescribe slip rates along the fault (e.g., Ameri et al., 2012; Frankel, 1991; Gallovič, 2016; Graves & Pitarka, 2016). Their simplicity and tractability justify their widespread use despite being possibly incompatible with rupture dynamics. Nevertheless, applications of kinematic modeling identify essential features required to fit earthquake ground motions. For example, the radiation of high-frequency waves must be sustained throughout the whole rupture process duration, have an omega-square spectrum, and be significantly incoherent to weaken high-frequency directivity (e.g., Bernard et al., 1996; Gallovič & Burjánek, 2007; Pacor et al., 2016).

Dynamic rupture modeling is a viable, physically consistent alternative. Although it has been proven successful for modeling low-frequency (<1 Hz) data (e.g., Ma et al., 2008; Olsen et al., 2008), it has several limitations that

Writing – original draft: F. Gallovič, Ľ. Valentová
Writing – review & editing: F. Gallovič, Ľ. Valentová

prevent broader applicability in practice where simulations toward broadband frequencies (5–10 Hz) are required. Dynamic simulations quickly become numerically overwhelming when aiming at higher frequencies and large magnitude earthquakes. Therefore, dynamic simulations are typically used for low-frequency ground-motion modeling and combined with stochastic Green's functions at high frequencies (Akinci et al., 2017; Galvez et al., 2021). The dynamic models are also used to guide kinematic models. For example, the observed constant stress-drop scaling of static crack models is the basis of composite earthquake models (Boatwright, 1988; Frankel, 1991). Irikura and Miyake (2011) introduced a kinematic model based on inhomogeneous static stress-drop distribution with high-slip asperities generating strong motions in low background slip. Dynamic models have also been used to infer statistical dependencies of selected rupture parameters (slip, slip rates, rupture velocity) to develop so-called pseudo-dynamic models, kinematic models that emulate fully dynamic rupture simulations (Guatteri et al., 2004; Mai et al., 2017; Mena et al., 2012; Savran & Olsen, 2020; Schmedes et al., 2013; Song et al., 2014; Tinti et al., 2005). Recently, Pitarka et al. (2022) used dynamic rupture modeling to improve their kinematic modeling of the M7.1 2019 Ridgecrest, California, earthquake by introducing smooth slip-rate functions at shallow depths.

Introducing high-frequency radiation in dynamic rupture models to simulate broadband data (0–10 Hz) is a challenging problem. As also demonstrated here, simple elliptical models with constant or smooth dynamic parameters do not generally radiate an omega-square source spectrum, but instead generate depleted high-frequency strong ground motions (Kaneko & Shearer, 2015; Madariaga, 1976; Oral et al., 2022). Madariaga (1977) associated local omega-square radiation with abrupt changes in rupture velocity due to, for example, frictional or stress heterogeneity (Pulido & Dalguer, 2009). Numerical experiments with self-similar initial stress distributions along planar faults (keeping frictional parameters constant or smooth) improve the high-frequency radiation, but still not enough, mainly for frequencies above 1–2 Hz (e.g., Andrews & Ma, 2016; Baumann & Dalguer, 2014; Oral et al., 2022; Ripperger et al., 2007). Note that although Valentová et al. (2021) considered all dynamic parameters to vary smoothly along the fault, they still underestimated spectral accelerations (SAs) above 1–2 Hz with respect to a ground motion model (GMM, Boore et al., 2014). The variations were either not strong enough or spatially correlated, suggesting that ad-hoc spatial variability does not guarantee sufficiently strong high-frequency source radiation.

The effects of sharp changes in fault geometry (kinks, roughness) represent a viable solution to the high-frequency source radiation issue (e.g., Adda-Bedia & Madariaga, 2008; Dunham et al., 2011). Shi and Day (2013) and Withers et al. (2019) performed numerical experiments with 3D nonplanar (rough) faults, obtaining omega-square source spectrum, complex radiation, and synthetics compatible with GMM up to 5 Hz. The geometrical fault roughness introduces rupture bursts of decelerating and accelerating rupture (up to super-shear speeds) that are not observed on geometrically planar fault models with smooth properties (i.e., Bruhat et al., 2016). Nevertheless, self-consistently accounting for small-scale fault roughness and other effects requires powerful supercomputers (Shi & Day, 2013; Taufiqurrahman et al., 2022), still preventing widespread use in ground motion studies where many rupture scenarios are needed. Moreover, as Beeler (2023) notes, geometrical roughness assumed in dynamic rupture modeling still oversimplifies the role of natural shear zone structure in earthquake faulting at short wavelengths.

A promising alternative to improve high-frequency radiation is introducing fractal stress and frictional properties, as also suggested by in-situ fault rock investigations (Miyamoto et al., 2022). Mikumo and Miyatake (1978) numerically demonstrated how non-uniform friction results in irregular rupture propagation. Ide and Aochi (2005) introduced a model with hierarchical slip-weakening distance D_c in the slip-weakening friction law (Figure 1a) on a planar fault, based on laboratory experiments with rough frictional surfaces and theoretical reasoning by Ohnaka (2003). Therein, D_c represents the size of a "local asperity" due to the unmodelled/neglected small-scale fault roughness with a self-affine fractal distribution. Their D_c map is generated using a random distribution of circular patches along the fault with number-size distribution following the power law of natural fault topographies. In the slip-weakening friction, fracture energy G_c (energy rate required to advance the rupture) is proportional to slip-weakening distance D_c and strength of the fault. Since Ide and Aochi (2005) considered constant strength, their G_c followed the same distribution as D_c, and thus G_c was connected to the fractal dimension of the fault topography, too. Using theoretical considerations from fracture mechanics, Ripperger et al. (2007) explain why the variability of fracture energy affects the rupture propagation complexity more than the variability of initial stress: since the crack tip equation of motion involves stress intensity factor, which is evaluated as an integral of past initial stresses, and a local value of G_c, the initial stress affects the rupture propagation more smoothly.

21699356, 2023, 6, Downloaded from https://agupubs.onlinelibrary.wiley.com/doi/10.1029/2023JB026506 by Charles University, Wiley Online Library on [15/01/2024]. See the Terms and Conditions (https://onlinelibrary.wiley.com/terms-and-conditions) on Wiley Online Library for rules of use; OA articles are governed by the applicable Creative Commons License

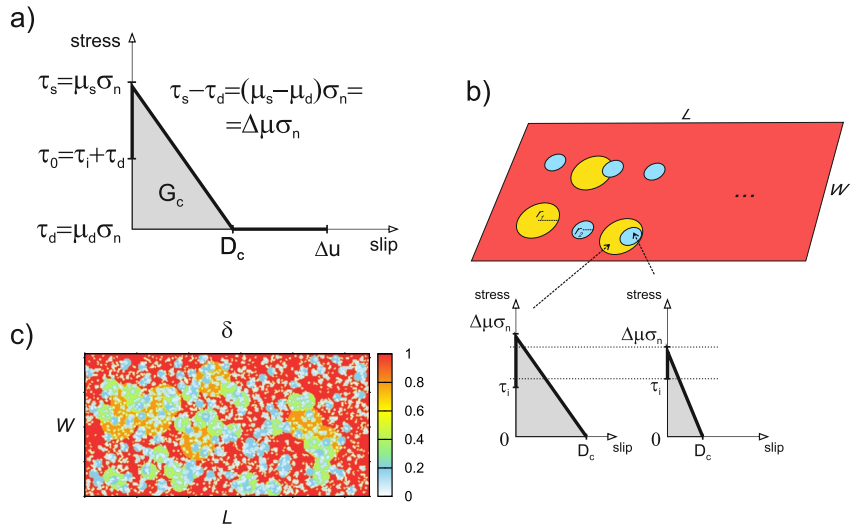

Figure 1. Schematics of the dynamic rupture model considered in this paper. (a) Diagram illustrating the slip-weakening friction law (Andrews, 1976; Palmer & Rice, 1973) with the following notation: initial stress τ_0, dynamic stress τ_d, prestress above dynamic stress τ_i, strength τ_s, static friction coefficient μ_s, dynamic friction coefficient μ_d, normal stress σ_n, slip-weakening distance D_c, final slip Δu, fracture energy G_c (Equation 1), and friction drop $\Delta\mu = \mu_s - \mu_d$. (b) Scheme of the template consisting of fractal patches. Each patch is characterized by scaled dynamic parameters as illustrated in the friction law diagrams below (see text). (c) An example of template δ used to alter a smooth original dynamic rupture model (see text).

Ide and Aochi (2005) proposed that their model explains many macroscopic properties of earthquakes, such as magnitude-frequency and magnitude-duration scaling laws. Okuda and Ide (2018) showed that the hierarchical rupture growth predicted by the Ide and Aochi's model is compatible with the observed weak initial parts of the waveforms; see also Ide (2019). In this model, the scaling of fracture energy with magnitude (e.g., Abercrombie & Rice, 2005) is interpreted as being due to the advancing rupture penetrating areas with progressively larger G_c. In addition, Renou et al. (2022) showed that the Ide and Aochi's model reproduces general characteristics of the rupture acceleration (development) phase empirically inferred by Renou et al. (2019).

The original model of Ide and Aochi (2005) was defined as fractal and random at all scales without any deterministic component. In practical applications, it will be helpful to preserve the large-scale properties of the model imposed in a deterministic way using, for example, low-frequency dynamic source inversions (Aochi & Twardzik, 2020; Fukuyama & Mikumo, 1993; Gallovič et al., 2020; Herrera et al., 2017; Peyrat & Olsen, 2004; Ruiz & Madariaga, 2013) or a generator of low-frequency dynamic scenarios (Aochi & Ide, 2014; Aochi & Ulrich, 2015; Harris et al., 2021; Valentová et al., 2021). Therefore, here we aim to introduce random small-scale perturbations to large-scale (low-frequency) dynamic rupture models, requiring:

- the high-frequency radiation is produced throughout the whole rupture propagation,
- the moment rates and the apparent moment rates have omega-square Fourier spectra,
- for different random realizations of the small-scale perturbations, the large-scale rupture propagation and low-frequency radiation are affected as little as possible.

We propose such a model, building upon the Ide and Aochi (2005) approach, taking advantage of introducing the effects of fractal rupture surface while keeping the efficiency of the simulations on a planar fault. To intensify the incoherence in the rupture propagation, we introduce additional variations of stress and strength correlated with those of D_c.

The rest of this paper is structured as follows. After introducing the approach, we demonstrate its performance on a smooth elliptical M_w 6.3 dynamic model and a relatively smooth dynamic model of the 2016 M_w 6.2 Amatrice earthquake inferred by a low-frequency data inversion. We demonstrate that the required properties specified above are satisfied and that the small-scale variations lead to an improved fit of real-data recordings of the Amatrice earthquake and Central Italy GMM in a broad frequency range (0–10 Hz).

21699356, 2023, 6, Downloaded from https://agupubs.onlinelibrary.wiley.com/doi/10.1029/2023JB026506 by Charles University, Wiley Online Library on [15/01/2024]. See the Terms and Conditions (https://onlinelibrary.wiley.com/terms-and-conditions) on Wiley Online Library for rules of use; OA articles are governed by the applicable Creative Commons License

21699356, 2023, 6, Downloaded from https://agupubs.onlinelibrary.wiley.com/doi/10.1029/2023JB026506 by Charles University, Wiley Online Library on [15/01/2024]. See the Terms and Conditions (https://onlinelibrary.wiley.com/terms-and-conditions) on Wiley Online Library for rules of use; OA articles are governed by the applicable Creative Commons License

2. Method

We assume that the shear stress evolution on the fault plane is governed by the slip-weakening friction law (Andrews, 1976; Palmer & Rice, 1973; see the diagram illustrating the friction law in Figure 1a). The stress increases from prestress τ_0 until it reaches strength τ_s. With increasing fault slip, the frictional stress then decreases linearly with increasing slip up to characteristic slip D_c, after which the strength remains constant at its dynamic value τ_d (considered here constant along the fault). In the slip-weakening friction law, fracture energy G_c, here the same as breakdown work density, is the energy per unit area expended in the rupture process to weaken the fault from static to dynamic friction while the slip reaches D_c (Day, 1982; Kanamori & Brodsky, 2004). Fracture energy for the slip-weakening friction reads (see Figure 1a)

$$G_c = \frac{1}{2}(\tau_s - \tau_d)D_c, \tag{1}$$

The S-parameter (also called strength parameter), expressing the strength excess to stress drop ratio, was defined by Das and Aki (1977) as

$$S = \frac{\tau_s - \tau_0}{\tau_0 - \tau_d}. \tag{2}$$

Friction drop $\Delta\mu$ is defined as

$$\Delta\mu = (\tau_s - \tau_d)/\sigma_n \tag{3}$$

where σ_n is the normal stress (see Figure 1a).

We assume a deterministic rupture model at the scale of the fault size to be known a priori. The showcase tests are (a) an ad-hoc dynamic crack model with approximately constant rupture velocity and (b) a dynamic model inferred by a low-frequency dynamic source inversion. For the smooth large-scale dynamic models, we devise small-scale random fractal perturbations of the dynamic parameters to enhance their high-frequency radiation, as explained in the Introduction. The minimum wavelength of the smooth model thus represents the characteristic length scale at which the fractal distribution breaks.

We first introduce a random fractal template to generate variations of D_c, which follows the model of Ide and Aochi (2005). To intensify the resulting incoherence of the rupture propagation, we apply the same realization of the fractal template to introduce variations of also strength and initial stress, thus being correlated with D_c. Eventually, we combine the fractal variations of the dynamic parameters with the large-scale dynamic model.

2.1. Fractal Template

Ide and Aochi (2005) introduced a fractal fracture energy model composed of overlapping randomly distributed multiscale circular patches with a number-size distribution of fractal dimension $D = 2$,

$$N(r) \propto r^{-D}. \tag{4}$$

They proposed that the characteristic slip-weakening distance inside each patch is proportional to the radius of the patch, and used the minimum slip-weakening distance over the overlapping patches. They realized the distribution by discrete patch levels, $n = 1 \ldots n_{\text{levels}}$, where level $n = 0$ corresponds to the background (parts of the fault not overlapped by the patches). The radius of the patches at level n is

$$r_n = 2^{-n} r_0, \tag{5}$$

and the number of n-level patches equals

$$N_n = 2^{Dn} N_0. \tag{6}$$

Here r_0 and N_0 are parameters of the distribution.

We follow this approach to build our non-dimensional function, called template δ, to be applied to a smooth model. The template is composed of randomly distributed circular patches on a unit background on the fault plane as described above. We assume the n-th level patch has value $\delta_n = r_n/r_0 = 2^{-n}$, so that the background value

21699356, 2023, 6, Downloaded from https://agupubs.onlinelibrary.wiley.com/doi/10.1029/2023JB026506 by Charles University, Wiley Online Library on [15/01/2024]. See the Terms and Conditions (https://onlinelibrary.wiley.com/terms-and-conditions) on Wiley Online Library for rules of use; OA articles are governed by the applicable Creative Commons License

$\delta_0 = 1$. Since the patches may overlap, the smallest patch δ_n value is considered as δ at each point on the fault. For an illustration of the template construction, see Figure 1b.

The background parameters r_0 and N_0 correspond to the properties of the whole fault ($r_0 \sim$ fault size, $N_0 = 1$). However, in our application, the template will be superposed on a large-scale dynamic model, whose characteristics are to be preserved (see Introduction). Therefore, the zero-level parameters r_0 and N_0 need to be smaller. By numerical experimenting (see also Discussion), we found that suitable values of r_0 and N_0 for a fault of length L and width W are

$$r_0 = {}^1\!/\!_8 \min(L, W), \tag{7}$$

and

$$N_0 = {}^L\!/\!_W. \tag{8}$$

An example of the fractal template δ is shown in Figure 1c. Table S1 in Supporting Information S1 presents a pseudocode describing the template generation procedure.

2.2. Perturbation of a Smooth Model by the Fractal Template

Denoting the smooth distribution of slip-weakening distance D_c^{smooth}, the perturbed model D_c is obtained simply by multiplication with the template δ,

$$D_c = c_D D_c^{\text{smooth}} \delta, \tag{9}$$

where c_D is a proportionality parameter (scalar constant).

For the initial stress τ_i and friction drop $\Delta\mu$ of the perturbed model (see Figure 1a), we propose variations following the same realization of the random template δ,

$$\tau_i = c_{\tau 1} \tau_i^{\text{smooth}} \left(1 - c_{\tau 2} \frac{\log \frac{\min(\delta)}{\delta}}{\log \min(\delta)} \right) \tag{10}$$

and

$$\Delta\mu = c_{\Delta\mu 1} \Delta\mu^{\text{smooth}} \left(1 + c_{\Delta\mu 2} \frac{\log \frac{\min(\delta)}{\delta}}{\log \min(\delta)} \right) \tag{11}$$

where $c_{\tau 1}$ and $c_{\mu 1}$ are constant proportionality parameters. The formulas introduce perturbations to initial stress τ_i within 100% of $c_{\tau 1} \tau_i^{\text{smooth}}$ for the smallest patches and $(1 - c_{\tau 2}) \times 100\%$ for the background. Likewise, friction drop $\Delta\mu$ (i.e., strength) varies between 100% of $c_{\Delta\mu 1} \Delta\mu^{\text{smooth}}$ for the smallest patches and $(1 + c_{\Delta\mu 2}) \times 100\%$ for the background. The perturbations are thus correlated with perturbations in D_c, but the template is rescaled by the logarithms to represent relative perturbations rather than absolute ones (i.e., we do not apply any additional random variations). The general increase of strength and decrease of stress for a given δ ensures that no additional nucleating areas where prestress exceeds strength will be introduced in the perturbed model. In contrast to D_c, the perturbation in strength and initial stress is locally smaller, the smaller δ is, that is, the smaller is the size of the template patch (see also the schematic friction diagrams in Figure 1b). Note that the large strength and D_c at the largest patches, which increase fracture energy G_c, are partially compensated by the decrease of strength and D_c at the superposed smaller patches. This approximate preservation of average G_c is crucial not to alter the large-scale rupture propagation, which is controlled by the fracture energy in the first place (Guatteri & Spudich, 2000).

Regarding the particular choice of the parameters, larger $c_{\tau 2}$ and $c_{\Delta\mu 2}$ decrease the initial stress and increase strength, respectively, thus they both tend to suppress the rupture. Values of $c_{\tau 1}$ and $c_{\Delta\mu 1}$ have to be selected with caution because nucleations at other parts of the fault can appear if different from 1. Making c_D larger than 1 also suppresses the rupture due to increasing the fracture energy. Nevertheless, suitable values are a matter of individual application and thus we consider them as tuning parameters.

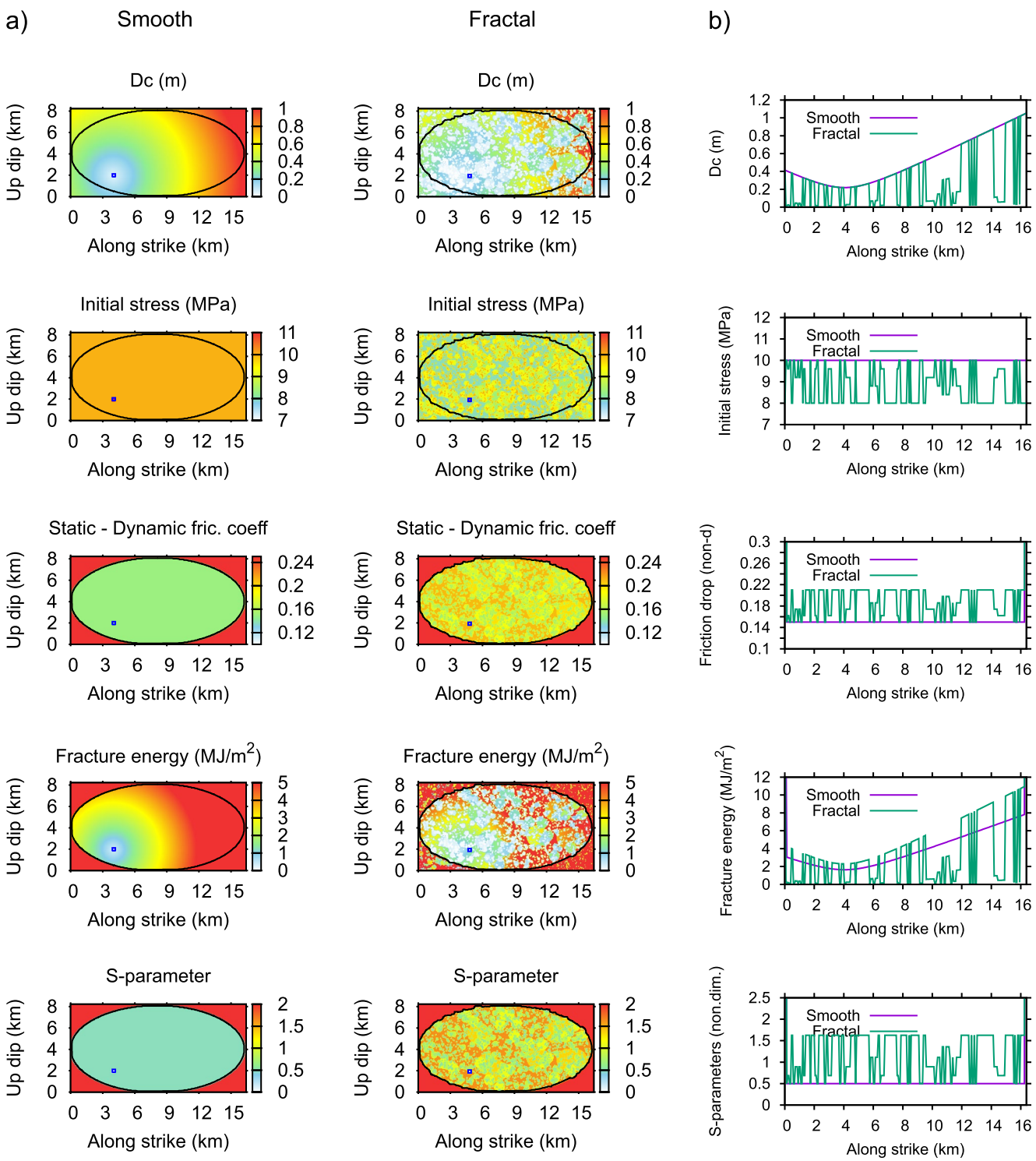

Figure 2. Dynamic rupture parameters of the elliptical source model example. (a) Along-fault distribution of parameters (see legends) for smooth and fractal dynamic models, respectively. Blue line delineates the negative strength excess (nucleation) area. Black line is the contour of final slip distribution dictated by the prescribed high-strength elliptical boundary. (b) Cross-sections of the respective parameters through the middle of the fault, see legend.

As an example, Figure 2a shows the smooth distribution of the slip-weakening distance, initial stress, and strength drop together with their perturbed counterparts, assuming the template of Figure 1c and parameters listed in Table 1. The cross-sections shown in Figure 2b further illustrate the resulting variability of the dynamic parameters.

21699356, 2023, 6, Downloaded from https://agupubs.onlinelibrary.wiley.com/doi/10.1029/2023JB026506 by Charles University, Wiley Online Library on [15/01/2024]. See the Terms and Conditions (https://onlinelibrary.wiley.com/terms-and-conditions) on Wiley Online Library for rules of use; OA articles are governed by the applicable Creative Commons License

21699356, 2023, 6, Downloaded from https://agupubs.onlinelibrary.wiley.com/doi/10.1029/2023JB026506 by Charles University, Wiley Online Library on [15/01/2024]. See the Terms and Conditions (https://onlinelibrary.wiley.com/terms-and-conditions) on Wiley Online Library for rules of use; OA articles are governed by the applicable Creative Commons License

Table 1
Model and Computational Parameters Considered for the M_w 6.3 Elliptical and 2016 M_w 6.2 Amatrice Earthquake Models

Parameter	Elliptical	Amatrice
General		
Fault mechanism (strike/dip/rake)	–	155°/45°/−85°
Fault dimensions (length × width)	16.384 km × 8.192 km	30 km × 14 km
Fault top depth	–	0 km
Normal stress	100 MPa	8.5 MPa/km
FD3D_TSN		
Spatial discretization	32 m	30 m
FD half-domain grid size (along strike × normal × along-dip)	512 × 300 × 256	1,000 × 200 × 466
Duration of slip-rate functions	10 s	12 s
Time step	0.001 s	0.0005 s
Maximum useable frequency	10 Hz	10 Hz
Parameterization of the fractal variations		
Discretization grid (along-strike × along-dip)	257 × 129	385 × 225
Number of fractal levels n_{levels}	5	5
Proportionality parameters c_D, $c_{\tau 1}$, $c_{\Delta\mu 1}$	1	1
Initial stress perturbation parameter $c_{\tau 2}$	0.2	0.2
Strength perturbation parameter $c_{\Delta\mu 2}$	0.4	0.4

Note. Some parameters do not apply to the elliptical model, which is considered in a homogeneous space.

2.3. Modeling Rupture Propagation and Seismic Waveforms

We utilize freely available dynamic earthquake rupture modeling software FD3D_TSN (Premus et al., 2020). It employs a fourth-order finite-difference method to solve the elastodynamic equation on a 3D regular staggered grid with traction-at-split-node implementation of the frictional boundary condition at the fault surface (Dalguer & Day, 2007). Artificial absorbing boundaries are realized by perfectly matched layers (PML, Berenger, 1994) in a split formulation (Kristek et al., 2009). An optional free surface is implemented using the stress imaging technique (Graves, 1996). The code utilizes GPU acceleration to speed up the simulations significantly. It was validated within Southern California Earthquake Center (SCEC) community benchmarks (Harris et al., 2018), and employed in dynamic inversions (Gallovič et al., 2019a, 2019b, 2020; Kostka et al., 2022) and scenario simulations (Gallovič & Valentová, 2020; Valentová et al., 2021).

Waveforms can be calculated following the representation theorem by convolving the slip rates resulting from the dynamic simulations with Green's functions (GFs). Here we use GFs pre-calculated for a 1D layered velocity model using Axitra (Cotton & Coutant, 1997). Nevertheless, more realistic GFs calculated in a 3D medium can also be used, or the resulting kinematic model (slip rates) can be implemented in any 3D wave propagation simulation. In this way, complex wave propagation phenomena such as basin effects or scattering in random media could be incorporated in the synthetics.

3. Results

Here we present two showcase examples, comparing smooth models with their perturbed counterparts and illustrating how the requirements specified in the Introduction are fulfilled. The first example assumes a smooth M_w 6.3 elliptical rupture model and demonstrates the performance and stability of the proposed random fractal perturbations. In the second application, we superimpose the fractal perturbations to a smooth dynamic rupture model of the 2016 M_w 6.2 Amatrice earthquake inferred by low-frequency (<0.5 Hz) inversion of near-source seismograms. The second example illustrates the performance of the proposed approach in more realistic applications, including comparison with broadband data and an empirical GMM. For the sake of simplicity, we set the

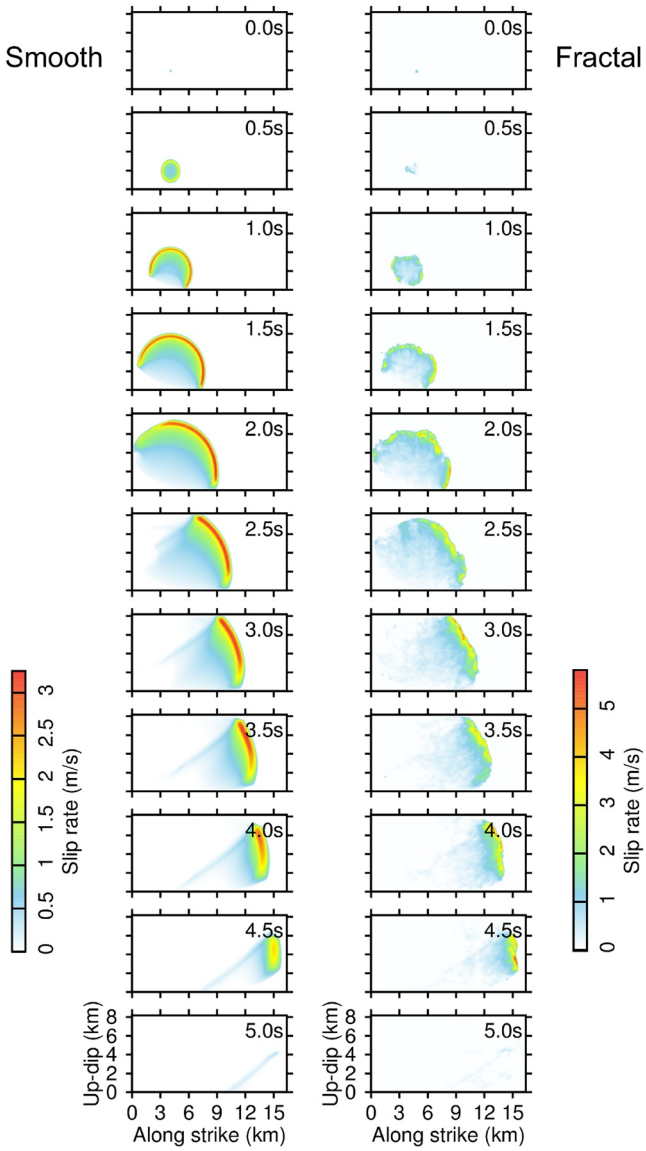

Figure 3. Snapshots of the rupture propagation for the elliptical source model (see also Movie S1). The left and right panels correspond to models with smooth and fractal distributions of dynamic parameters, respectively (see Figure 2). Note the different color scales.

proportionality parameters c_D, $c_{\tau 1}$, and $c_{\mu 1}$ equal to 1 in both cases. The other parameters are summarized in Table 1.

3.1. Elliptical Model

We assume a planar fault governed by the slip-weakening friction law in a homogenous isotropic Poissonian medium with *P*-wave velocity $v_P = 6$ km and density $\rho = 2.71$ g/cm^3. We prescribe constant normal stress $\sigma_n = 100$ MPa, dynamic stress $\tau_d = 40$ MPa and frictional cohesion of 0.5 MPa everywhere on the fault. For the smooth model, we assume constant initial stress $\tau_i^{\text{smooth}} = 10$ MPa oriented upwards in Figure 2 and constant friction drop $\Delta\mu^{\text{smooth}} = 0.15$ (and thus constant strength $\tau_s^{\text{smooth}} = 55$ MPa) inside an ellipse with size corresponding to the size of the fault. The ellipse is delimited by a barrier with a high (unsurpassable) strength of 550 MPa.

We prescribe a linearly increasing slip-weakening distance from a small nucleation patch. Such a model generally allows an approximately constant rupture velocity (Aochi & Ide, 2004; Kaneko & Shearer, 2015; Oral et al., 2022) and a relatively small nucleation patch, preventing overly strong nucleation that would contaminate the rest of the spontaneously propagating rupture (Galis et al., 2015). We define an ad-hoc model with

$$D_c^{\text{smooth}}(\rho) = 0.05[\text{m}] + 0.08\rho[\text{km}], \tag{12}$$

where ρ is the distance from the assumed nucleation, see Figure 2. The nucleation is realized by setting initial stress 10% above the strength on a patch of 150 m × 150 m at point 4.096 and 2.048 km along strike and along dip, respectively.

The numerical discretization for FD3D_TSN is listed in Table 1. We note that a relatively small box surrounding the fault minimizing the computational demands of the rupture simulation is assumed thanks to the efficacy of the employed PML nonreflecting boundaries. The dynamic parameters are defined on an about twice coarse grid as the finite-difference grid (see Table 1). We resample the values using bilinear interpolation. The dynamic simulation is finished in about 4 min on a single Nvidia RTX-2070 graphic card.

The dynamic parameters on the finite-difference grid are shown in Figure 2a (left), including the fracture energy (Equation 1) and the *S*-parameter (Equation 2). In this setting, the fracture energy increases linearly away from the nucleation. The S-parameter inside the ellipse has a constant value of 0.5, considered low-to-mid in parametric studies and corresponding to more energetic, possibly supershear ruptures if D_c was constant (e.g., Galis et al., 2015).

Figure 3 (left) and Movie S1 show snapshots of the resulting rupture evolution, demonstrating the prescribed weak nucleation and a smoothly propagating rupture at an approximately constant speed, which is slightly higher in the in-plane (up-dip) than in the anti-plane (along-strike) direction (see also rupture velocity in Figure 4a left). The constant speed is preserved because the fracture energy suitably increases with distance. Kinematic parameters of the rupture in Figure 4a (left) show crack-like static slip distribution. The resulting moment magnitude of this event is M_w 6.3.

Next, we add fractal variations to the dynamic parameters following Equations 9–11 with parameters listed in Table 1. The perturbed distributions are shown in Figure 2a (right). Note that the perturbations implicitly modify both fracture energy G_c and the *S*-parameter. In this case, we slightly shift the prescribed nucleation to the nearest patch with the smallest D_c. Figure 2b shows cross-sections through the middle of the fault, comparing the smooth and fractal parameters for ease of demonstration.

21699356, 2023, 6, Downloaded from https://agupubs.onlinelibrary.wiley.com/doi/10.1029/2023JB026506 by Charles University, Wiley Online Library on [15/01/2024]. See the Terms and Conditions (https://onlinelibrary.wiley.com/terms-and-conditions) on Wiley Online Library for rules of use; OA articles are governed by the applicable Creative Commons License

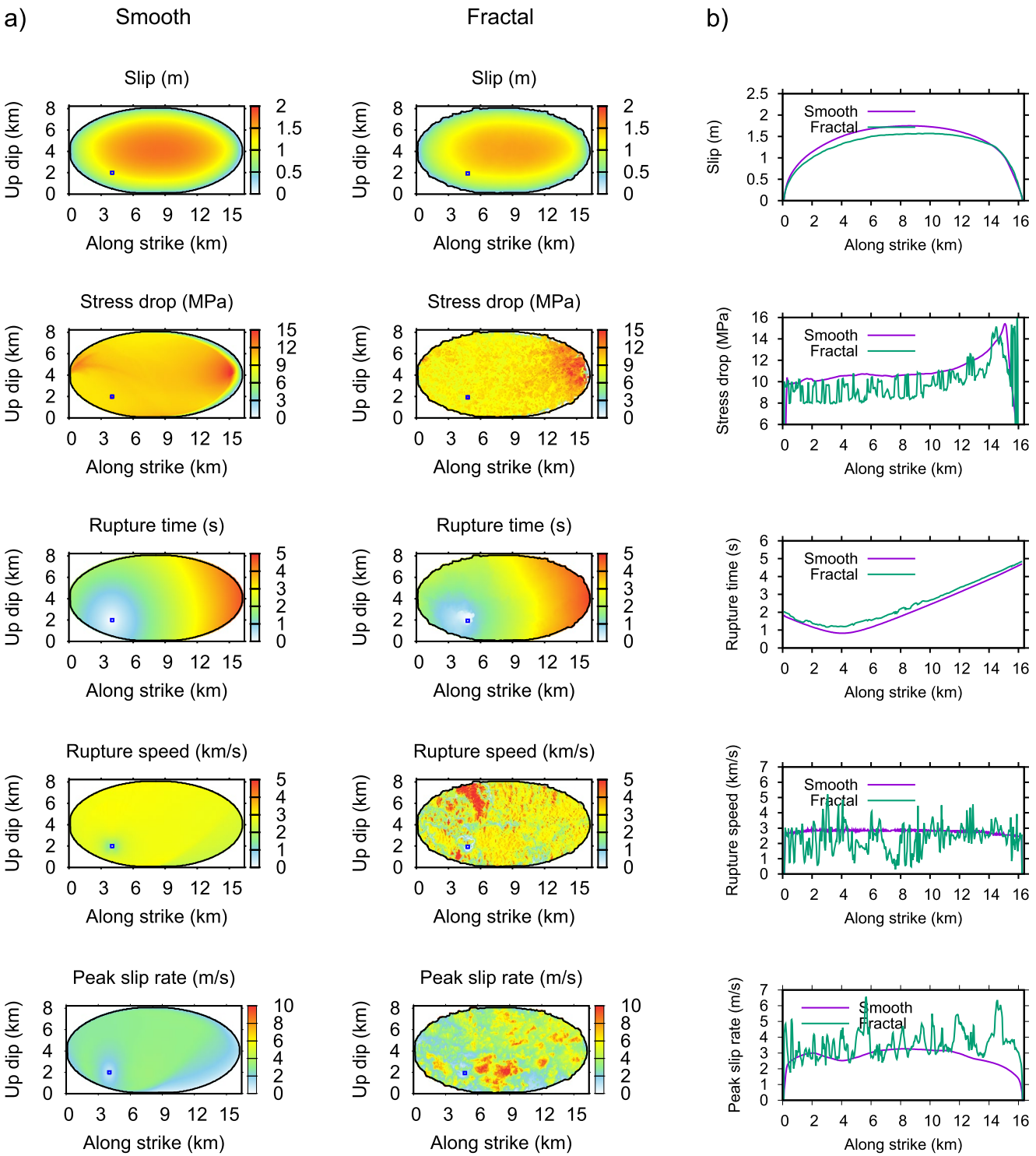

Figure 4. Kinematic rupture parameters of the elliptical source model. (a) Along-fault distribution of parameters (see legend) for smooth and fractal dynamic models, respectively (see Figure 2). Blue line delineates the negative strength excess (nucleation) area. Black line is the contour of final slip distribution. (b) Cross-sections of the respective parameters through the middle of the fault, see legend.

Figure 3 (right) and Movie S1 show the snapshots of the rupture propagation. Starting from the small nucleation area with low G_c, the rupture finds its way through similar low G_c areas. As it grows further, the energy release rate increases, surpassing the generally increasing fracture energy at the crack tip. The rupture could be stopped at large-G_c areas, but it gains an additional push by triggering the overlaid small patches with smaller G_c and

21699356, 2023, 6, Downloaded from https://agupubs.onlinelibrary.wiley.com/doi/10.1029/2023JB026506 by Charles University, Wiley Online Library on [15/01/2024]. See the Terms and Conditions (https://onlinelibrary.wiley.com/terms-and-conditions) on Wiley Online Library for rules of use; OA articles are governed by the applicable Creative Commons License

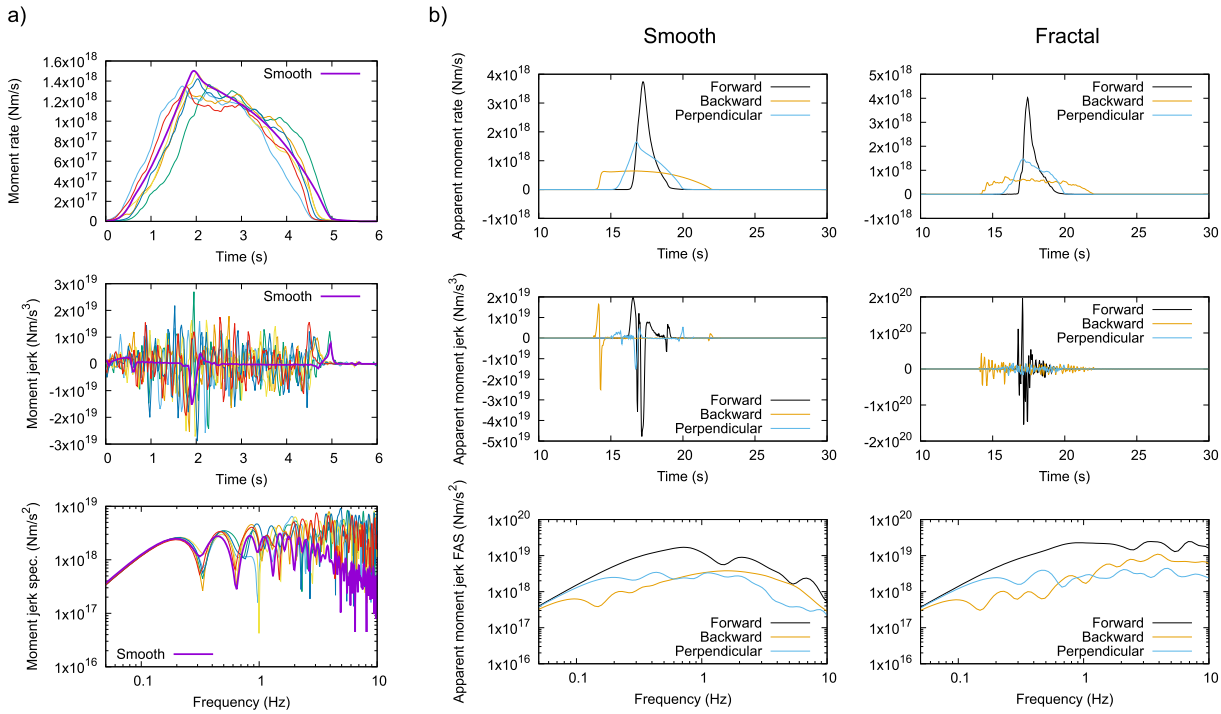

Figure 5. Analysis of the radiation of the elliptical dynamic source model. (a) Moment rate functions, their second-time derivatives (jerks), and spectra corresponding to the model with smooth parameters (thick line) and six random realizations of the fractal small-scale perturbations (thin lines). One of the realizations corresponds to the model presented in Figures 2–4. Note the high-frequency spectral plateau corresponding to omega-squared radiation of the fractal models within the entire rupture duration and the stability of the behavior concerning the random realization of the fractal perturbations. (b) Apparent moment rates, their second-time derivatives (jerks), and spectra for three receiver stations at 50 km distance from the fault center in the forward, backward, and perpendicular directions with respect to the predominant rupture propagation, assuming smooth (left) and one of the fractal (right) distributions of the dynamic rupture parameters. The fractal model is the same as in Figures 2–4. Note that the high-frequency omega-squared radiation is persistent within the apparent duration for all receivers, unlike in the case of the smooth model exhibiting stronger spectral decay and intervals of no high-frequency radiation.

strength, and larger stress drop. Due to the dependence of the strength on D_c, the rupture can also jump over areas with large G_c (and thus with larger strength) to a small patch with lower G_c and strength, becoming more energetic and eventually rupturing the previously bypassed area. We note that the peak slip rates of the fractal model can significantly exceed those of the smooth model.

In terms of kinematic rupture parameters shown in Figure 4, the slip distributions of the smooth and fractal models are alike. Contrarily, the stress drop, peak slip rate, and rupture speed of the fractal model are highly variable, including small areas of supershear rupture propagation. Wiggles on the rupture time distributions, best visible on the cross-section in Figure 4b, express the rupture jumps during the faulting.

Regarding the radiation of seismic waves, Figure 5a explores the seismic moment release rate calculated by integrating the slip rates along the fault up to 10 Hz. In addition to the smooth model, Figure 5a shows moment release rates for five different realizations of the random fractal perturbations (i.e., random spatial distribution of the patches). The apparent moment rates correspond to the far-field displacements, but the high-frequency effects are especially important for accelerations. The far-field accelerations correspond to the second time derivative of the moment release rate, hereinafter called moment jerk. Figure 5a shows that the smooth model produces only three significant peaks in the moment jerk related to the stopping phases from the rupture hitting the ellipse's left, top, and right edges. In contrast, the fractal models result in heterogeneous rupture propagation associated with episodes of abrupt changes of slip and rupture velocities, producing bursts of multiple peaks throughout the whole duration of the rupture process, which overlay the stopping phases. Figure 5a also shows the Fourier spectra of the moment jerks, further demonstrating the similarity of the spectra with the smooth model at low frequencies and the enhanced radiation of high-frequency energy of the fractal model, yielding omega-square spectral decay (expressed as a plateau in the moment jerk spectrum), in contrast to the smooth model with a faster decay. We point out that the

21699356, 2023, 6, Downloaded from https://agupubs.onlinelibrary.wiley.com/doi/10.1029/2023JB026506 by Charles University, Wiley Online Library on [15/01/2024]. See the Terms and Conditions (https://onlinelibrary.wiley.com/terms-and-conditions) on Wiley Online Library for rules of use; OA articles are governed by the applicable Creative Commons License

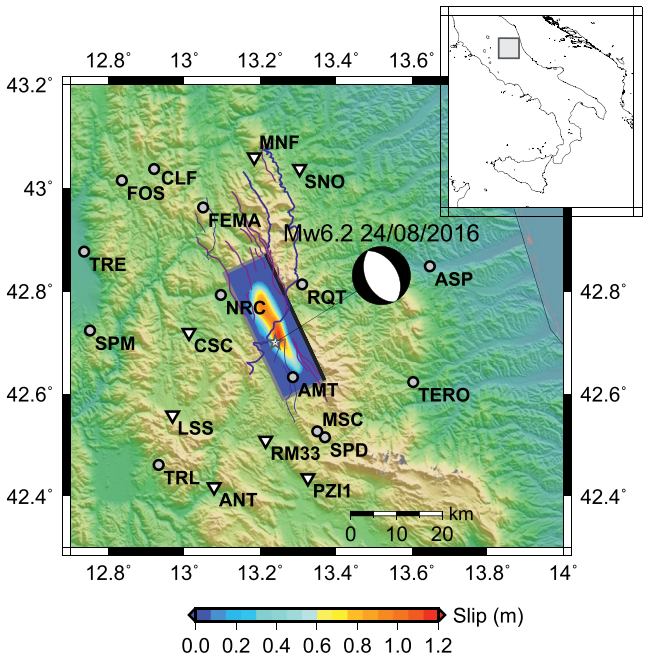

Figure 6. Map of the epicentral area of the 2016 Mw6.2 Amatrice earthquake. Star and beachball represent location epicenter and focal mechanism, respectively (Chiaraluce et al., 2017). Rectangle depicts the fault with its top edge in bold. Slip distribution of the inverted smooth dynamic model by Taufiqurrahman et al. (2022) is color-coded. Stations are marked by their codes, where inverted triangles denote those with weak site effects. Violet and blue curves correspond to active normal faults and Miocene-Pliocene thrusts, respectively; the bold blue curves mark the Sibillini Thrust Fault (Pierantoni et al., 2013). The area is depicted as the gray rectangle in the inset map of Italy.

same features are present for all the random realizations, demonstrating the stability of the proposed approach to enrich the smooth model by small-scale irregularities.

Similar behavior can be observed for the *S*-wave apparent source time functions (ASTF) for three virtual receivers located in the forward and backward rupture directions and perpendicular to the fault. Figure 5b shows the ASTFs and their second time-derivatives (apparent moment jerks) corresponding to far-field displacements and accelerations, respectively. Fourier spectra of the latter are displayed, too. The ASTFs exhibit the standard shortening of the apparent duration and increase of the peak amplitude for the forward directivity receiver for both the smooth and fractal models. Nevertheless, the fractal model is again associated with stronger high-frequency radiation expressed by the larger amplitudes of the apparent moment jerks and stable spectral plateau for all receivers' directions. We also point out the high-frequency radiation efficacy throughout the rupture process (best visible in the numerous moment jerk peaks) in contrast to the distinct three stopping phases of the smooth model.

3.2. The 2016 Amatrice (Italy) Earthquake

The M_w 6.2 Amatrice earthquake was the first of three mainshocks of the 2016 Central Italy seismic sequence (e.g., Chiaraluce et al., 2017; Cirella et al., 2018; Kheirdast et al., 2021; Pischiutta et al., 2020; Pizzi et al., 2017; Ragon et al., 2019; Tinti et al., 2016). Among many source studies, Gallovič et al. (2019b) inferred a dynamic rupture model using the dynamic source inversion technique, considering waveforms at frequencies below 1 Hz from 20 stations within 50 km from the fault (Figure 6). The dynamic parameters were considered heterogeneous along the fault, bilinearly interpolated from a 2.5 km × 2 km coarse grid of so-called control points. In the Bayesian source inversion, the control-point parameter values were optimized using a Markov Chain Monte Carlo approach. Here we adopt the starting model of Taufiqurrahman et al. (2022) from an updated inversion as the smooth model to be enriched by the small-scale fractal perturbations, see Figure 7.

We assume 500 random realizations of fractal templates (i.e., spatial distribution of the patches) and apply them to the smooth model following Equations 9–11, considering parameters in Table 1. We run the dynamic rupture simulation (see Table 1 for further details on numerical setup) for each realization and calculate waveforms, considering the 1D velocity model of Gallovič et al. (2019b) adapted roughly to a rock site with V_s 30 = 800 m/s by adding three shallow layers (Table 2). The dynamic simulation takes about 25 min on a single Nvidia RTX-2070 GPU. For each model, we evaluate the variance reduction to the real data downloaded from the Engineering Strong-Motion (ESM) database (Lanzano et al., 2021) at all stations in the frequency range of 0.05–0.50 Hz (i.e., the frequency range of the dynamic inversion). The best-fitting fractal model has a variance reduction VR = 0.60, about the same as the original smooth model. Figure 7 shows the dynamic parameters of the best-fitting model, including cross-sections, to appreciate the difference from the smooth model. As for the elliptical model, the fractal model of the Amatrice earthquake features substantial variations of all dynamic parameters following the given template.

Figure 8a and Movie S2 compare the rupture evolution of the smooth and fractal models. It demonstrates how the fractal properties introduce perturbations to the rupture propagation, including decoherence of the rupture front and advanced and delayed breakage of small-scale patches, as already described in the previous example. Still, the overall behavior (e.g., weak nucleation, bilateral rupture propagation) is in accord with the smooth model, explaining the agreement of the models in terms of low-frequency waveforms. Figure 8b displays slip rates of the smooth and fractal models at three selected points depicted in Figure 8a. They further demonstrate the diversity of effects of the fractal perturbations: rupture advance and a secondary peak at point 1, formation of multiple peaks at point 2 (above nucleation), and relatively simple increase of the peak slip rate at point 3.

21699356, 2023, 6, Downloaded from https://agupubs.onlinelibrary.wiley.com/doi/10.1029/2023JB026506 by Charles University, Wiley Online Library on [15/01/2024]. See the Terms and Conditions (https://onlinelibrary.wiley.com/terms-and-conditions) on Wiley Online Library for rules of use; OA articles are governed by the applicable Creative Commons License

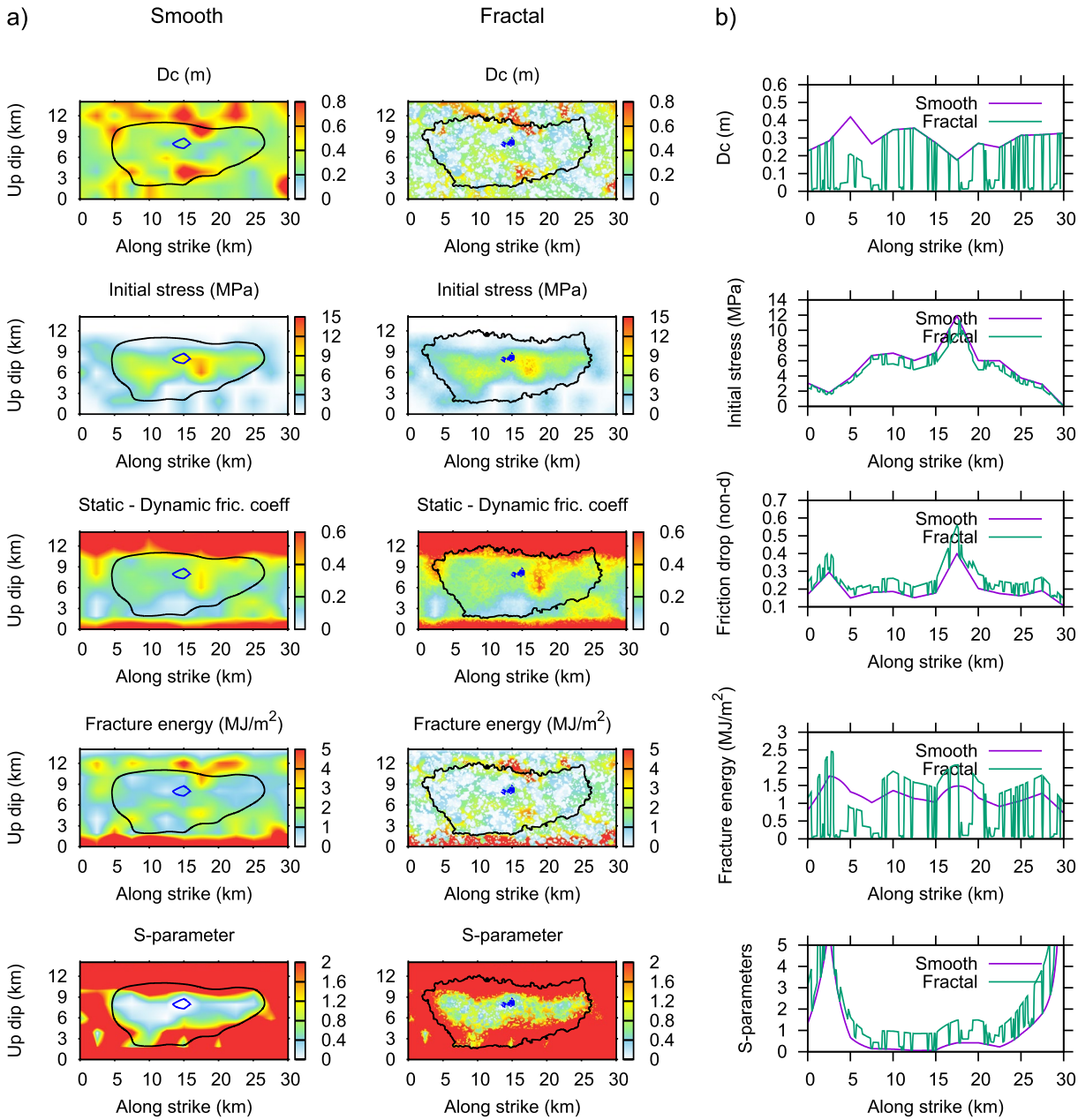

Figure 7. Dynamic rupture parameters of the Amatrice source model. (a) Along-fault distribution of parameters (see legend) for smooth and fractal dynamic models. Blue lines delineate the negative strength excess (nucleation) area. Note that the perturbations split the nucleation into many small areas in the fractal model. Black line is the contour of the final slip distribution (where the rupture stopped spontaneously). (b) Cross-sections of the respective parameters through the middle of the fault, see legend.

Figure 9 displays the distributions of slip, stress drop, rupture times, rupture speeds, and peak slip rates for the smooth and the best fractal model. A minimal change can be observed for the slip. Contrarily, the peak slip rates and rupture speeds exhibit substantial variations within the whole ruptured patch, including localized areas of supershear propagation. The wiggles in the rupture times further demonstrate the chaotic rupture evolution.

For the best fractal model, we recalculate seismograms up to 10 Hz. A comparison of vertical components of the synthetics for the smooth and fractal models with the real data at selected stations (with weak site effects, Lanzano et al., 2022, and near the fault) shown in Figure 10 demonstrates the impact of the rupture propagation complexity on seismic waveforms. For all stations and components see Figure S1 in Supporting Information S1. As observed for

21699356, 2023, 6, Downloaded from https://agupubs.onlinelibrary.wiley.com/doi/10.1029/2023JB026506 by Charles University, Wiley Online Library on [15/01/2024]. See the Terms and Conditions (https://onlinelibrary.wiley.com/terms-and-conditions) on Wiley Online Library for rules of use; OA articles are governed by the applicable Creative Commons License

Table 2
Velocity Model Considered for the Modeling of the 2016 Mw6.2 Amatrice Earthquake, Adapted From Ameri et al. (2012) by Adding Three Low-Velocity Subsurface Layers

Top depth (km)	V_p (km/s)	V_s (km/s)	ρ (g/cm^3)	Q_p	Q_s
0.00	1.49	0.80	1.90	50	50
0.06	2.23	1.20	1.90	100	100
0.16	3.16	1.70	2.00	100	100
1.00	4.83	2.60	2.84	400	200
2.00	5.76	3.10	2.94	400	200
5.00	6.51	3.50	3.15	400	200
27.0	7.00	3.80	3.26	600	300
42.0	7.80	4.20	3.50	800	400

the elliptical model, adding small-scale perturbations enhances high-frequency source radiation for all stations, including NRC and AMT lying above the fault. This enhancement is present in the P-wave group and early part of the S waves, improving their agreement with the observed data. We also quantify the fit using the Goodness-of-fit (GOF) metrics (Olsen & Mayhew, 2010), including peak ground velocity and displacement, SA, FAS, energy duration, and cumulative energy. The GOF values, specified in parentheses in Figure 10, are considerably larger for the fractal model for each waveform. The spectra demonstrate a good agreement of all waveforms at frequencies below 0.5 Hz. Although the fractal rupture properties amplify the synthetics at high frequencies for station SNO located toward the north of the fault, the synthetics still underestimate the observations. This issue may be related to the omission of the site effects and/or directivity effect improperly modeled by the original smooth dynamic model (a similar effect was also observed by Taufiqurrahman et al., 2022, employing the same smooth model). We point out that the high-frequency enhancement due to the rupture propagation complexity in the fractal model is effective even in near-field stations NRC and AMT, see Figure 10. We also note that for different realizations of the small-scale perturbations, the seismograms would have only differently distributed random high-frequency peaks that enhance the high-frequency spectrum by the same amount, as demonstrated for the elliptical moment for several random realizations of the fractal properties in Figure 5a.

Figure 11 compares the synthetics with the GMM by Sgobba et al. (2021) in terms of SAs at four frequencies (5, 2, 1, and 0.5 Hz), evaluated from the geometric mean of horizontal components. The SAs are about the same for both the smooth and fractal models at 0.5 Hz, agreeing with the GMM. Starting from 1 Hz, the SAs of the smooth model underestimate the GMM and feature larger (within-event) variability exceeding the total variability of the GMM. The fractal model remedies (a) the underestimation of the mean value due to its stronger high-frequency radiation, and (b) the overestimation of the within-event variability of the SAs above 1 Hz due to the weakened directivity effect. The latter is connected with the complex rupturing of the smaller overlapping patches in random directions in the fractal model. It agrees with the observed weakening of the directivity effects with increasing frequency above the corner frequency (Gallovič, 2016; Pacor et al., 2016) and with the widely used kinematic composite source models that inherently suppress the directivity by incoherent summation of subsource waveform contributions (Gallovič & Burjánek, 2007; Graves & Pitarka, 2010; Irikura & Miyake, 2011; Zeng et al., 1994).

Eventually, out of the 500 random fractal models, we select only those that fit the recordings with VR > 0.5 at frequencies 0.05–0.5 Hz (note that despite the perturbations also alter the nucleation area, most unsuccessful models are characterized by lower waveform fit despite having a satisfactory seismic moment). In Figure 12, we inspect the statistical properties of the 23 successful models in terms of their gross parameters, namely seismic moment, average rupture speed and stress drop, radiated and fracture energies, and radiation efficiency (Kanamori & Brodsky, 2004). Comparison with the smooth and best-fitting fractal models suggests agreement of all values within a factor of 2. For example, the moment magnitude of all models ranges between 6.2 and 6.33, and the radiation efficiency lies between 0.18 and 0.29. The mean stress drop of all the fractal models is ∼20% lower than that of the smooth model. This is dictated by how the initial stress is perturbed and the choice of constants in Equation 10. In our particular setting, the background value of the initial stress is decreased by about 20% due to considering $c_{\tau 1} = 1$ and $c_{\tau 2} = 0.2$ (see Table 1). The average stress drop might be increased back, if needed, by setting $c_{\tau 1}$ slightly above 1 to compensate for the initial stress decrease (while also adjusting strength constant $c_{\Delta\mu 1}$ in Equation 11 to avoid the prestress exceeding the initial stress outside the nucleation).

4. Discussion

4.1. Numerical Aspects of the Simulations

Ide and Aochi (2005) simulated rupture propagation using a boundary integral element method combined with a gradual enlargement of the computational domain as the rupture propagates by upscaling the model by renormalization and increasing the grid steps. This way, they could reach the smallest fractal patches of radius 22 m and $D_c \sim 1$ mm. Although we have a minimum radius of 110 m and $D_c \sim 1$ cm in our modeling, we can avoid that numerical trick and perform the calculation in a single run due to the highly efficient finite-difference

21699356, 2023, 6, Downloaded from https://agupubs.onlinelibrary.wiley.com/doi/10.1029/2023JB026506 by Charles University, Wiley Online Library on [15/01/2024]. See the Terms and Conditions (https://onlinelibrary.wiley.com/terms-and-conditions) on Wiley Online Library for rules of use; OA articles are governed by the applicable Creative Commons License

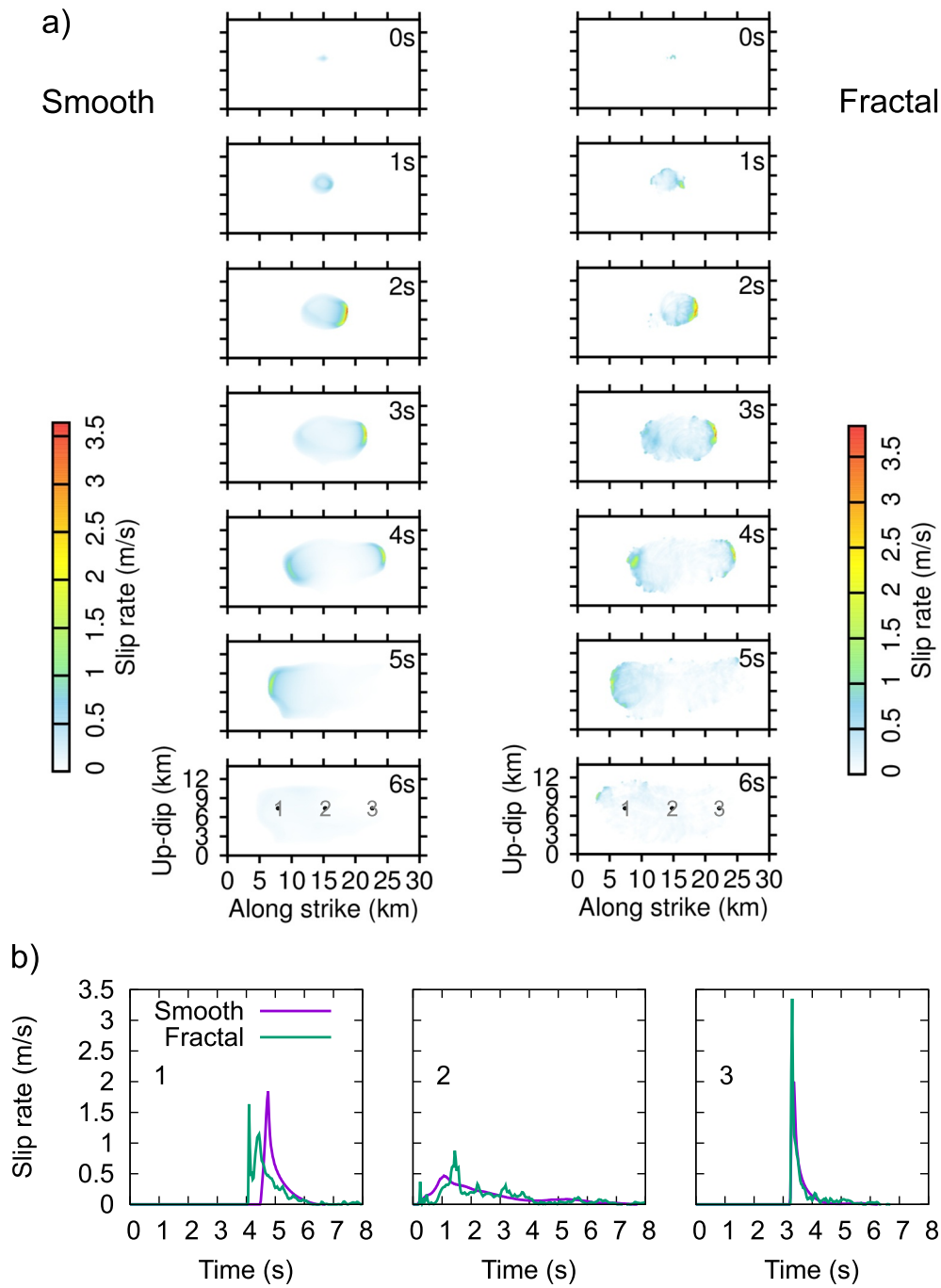

Figure 8. Rupture propagation for the Amatrice source model. (a) Snapshots corresponding to the models with smooth and fractal distributions of dynamic parameters (Figure 7), see also Movie S2. (b) Slip rates at three selected points depicted in the bottommost snapshots of panel (a).

code FD3D_TSN. Our simulations take about 25 min for the M_w 6.2 Amatrice earthquake rupture with a 10 s duration and precision up to 10 Hz on a single GPU. The speedup of the code stems mainly from the offload of computationally intensive calculation to a GPU accelerator and the implicit assumption of a vertical planar fault aligned with the finite-difference mesh (Premus et al., 2020).

We point out that the fractal dynamic model introduced here can be easily implemented in any dynamic rupture propagation code (see the pseudocode provided in Table S1 in Supporting Information S1). Thanks to using a

21699356, 2023, 6, Downloaded from https://agupubs.onlinelibrary.wiley.com/doi/10.1029/2023JB026506 by Charles University, Wiley Online Library on [15/01/2024]. See the Terms and Conditions (https://onlinelibrary.wiley.com/terms-and-conditions) on Wiley Online Library for rules of use; OA articles are governed by the applicable Creative Commons License

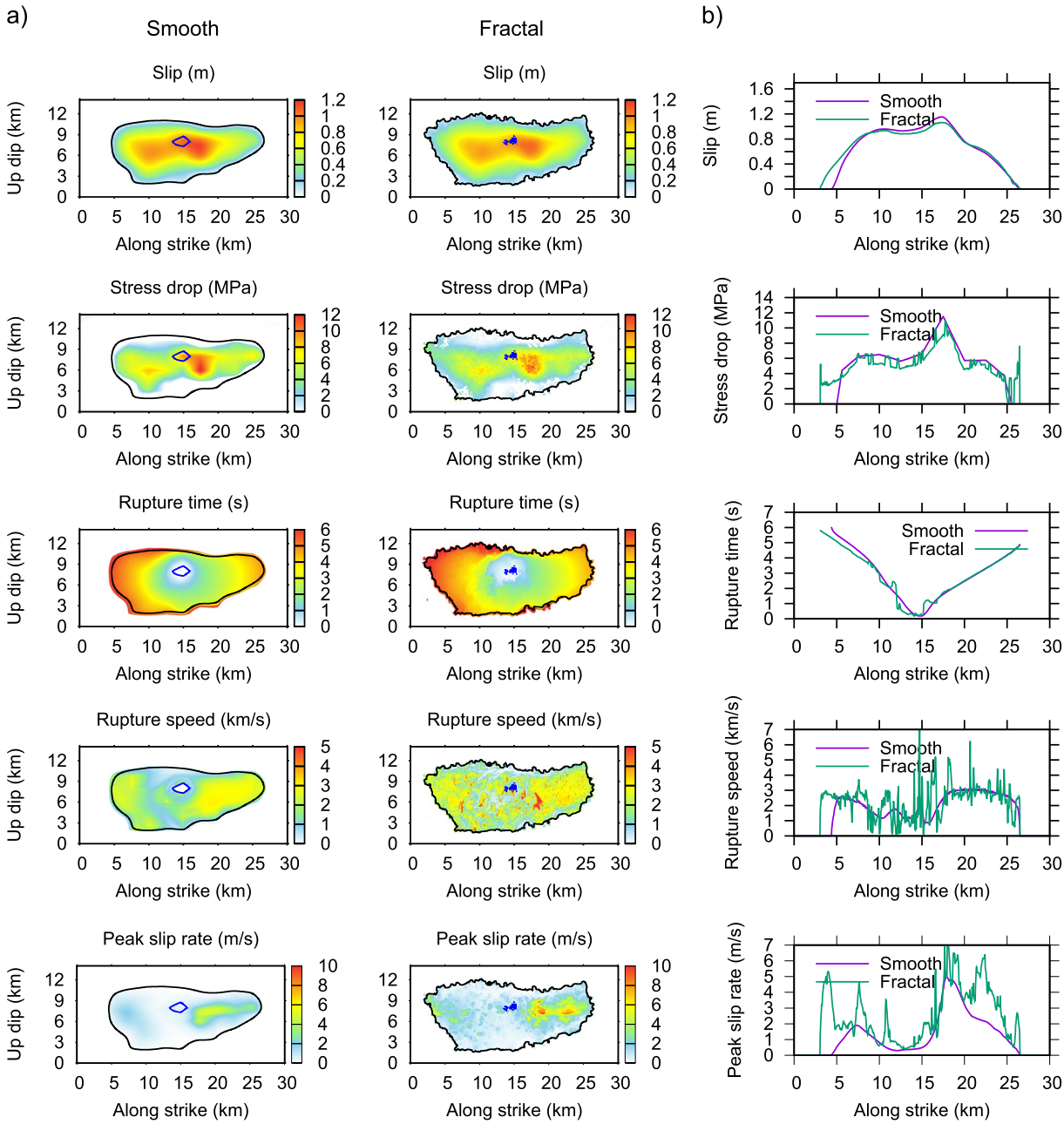

Figure 9. Kinematic rupture parameters of the Amatrice source model. (a) Along-fault distribution of parameters (see legend) for smooth and fractal dynamic models (see Figure 7). Blue lines delineate the negative strength excess (nucleation) area. Black line is the contour of final slip distribution. (b) Cross-sections of the respective parameters through the middle of the fault, see legend.

planar fault instead of complex small-scale nonplanar geometries, numerical simulations can be much less expensive. The proposed approach is thus readily applicable in physics-based ground motion predictions for scenario earthquakes in seismic hazard assessment.

4.2. Physical Interpretation of the Fractal Dynamic Model

Although our model is based on vast numerical experimenting, it warrants a physical interpretation. Ide and Aochi (2005) introduced the idea of the fractal distribution of D_c as a proxy to the effect of nonplanar fault topography. In particular, fracture energy G_c is considered to depend locally on the size of the macroscopic fault deflection. This is motivated by laboratory experiments and interpretations by Ohnaka (2003), who found that the

21699356, 2023, 6, Downloaded from https://agupubs.onlinelibrary.wiley.com/doi/10.1029/2023JB026506 by Charles University, Wiley Online Library on [15/01/2024]. See the Terms and Conditions (https://onlinelibrary.wiley.com/terms-and-conditions) on Wiley Online Library for rules of use; OA articles are governed by the applicable Creative Commons License

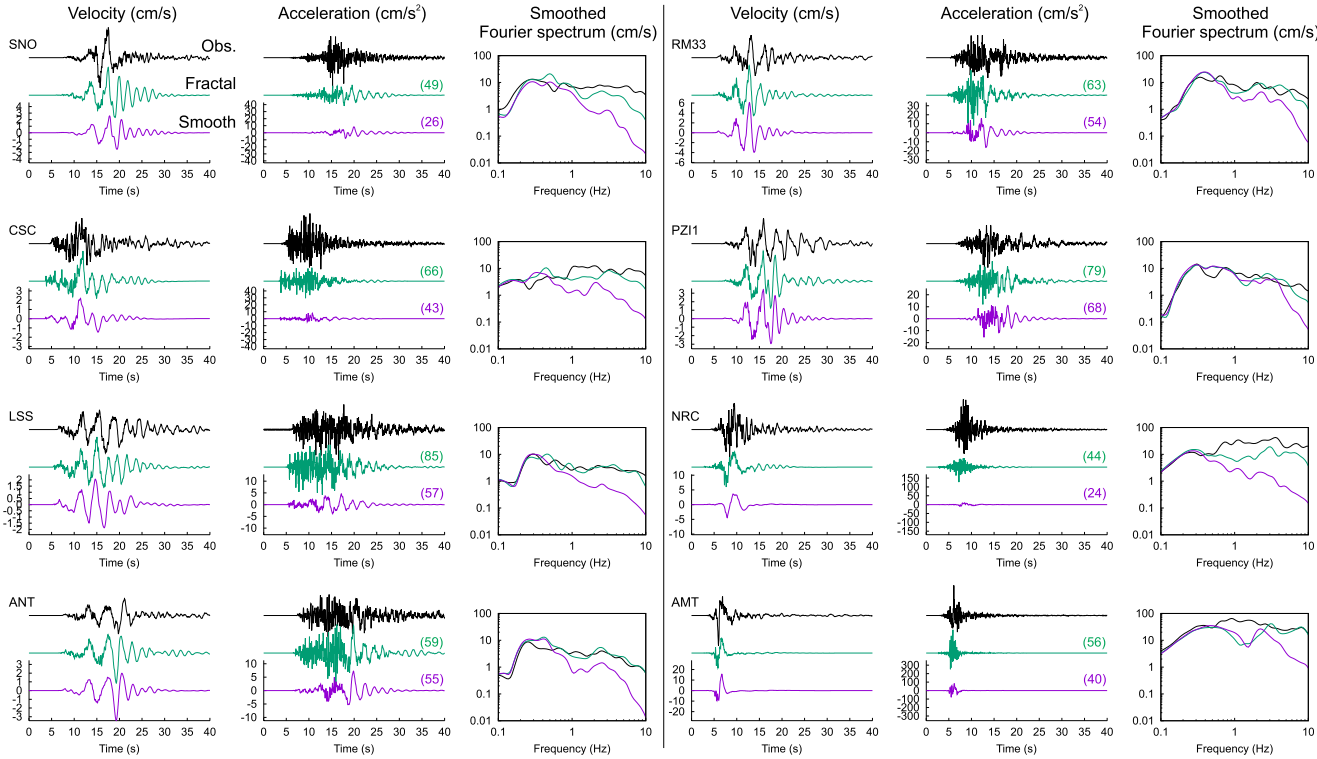

Figure 10. Comparison of vertical component seismograms (velocities, accelerations), and acceleration amplitude spectra of selected stations with relatively weak site effects (Lanzano et al., 2022) and near-fault stations (NRC, AMT), see Figure 6, in frequency range 0–10 Hz. Data are in black, while synthetics are green and violet for the fractal and smooth dynamic rupture models, respectively. Goodness-of-fit is displayed in parenthesis. For all stations and components see Figure S1 in Supporting Information S1.

fault roughness scales with D_c and $\mu_s/\Delta\mu$ (see Figure 1a). Considering no or limited variations in the static and dynamic friction coefficients, this model generally explains the scale-dependence of D_c, ranging from the order of meters for large earthquakes (Gallovič et al., 2019b, 2020; Ide & Takeo, 1997; Mikumo et al., 2003; Olsen et al., 1997) to the order of micrometers in laboratory experiments (Ohnaka, 2003; Scholz, 2002). The model also interprets the observed scaling of fracture energy as due to the rupture penetrating areas with progressively

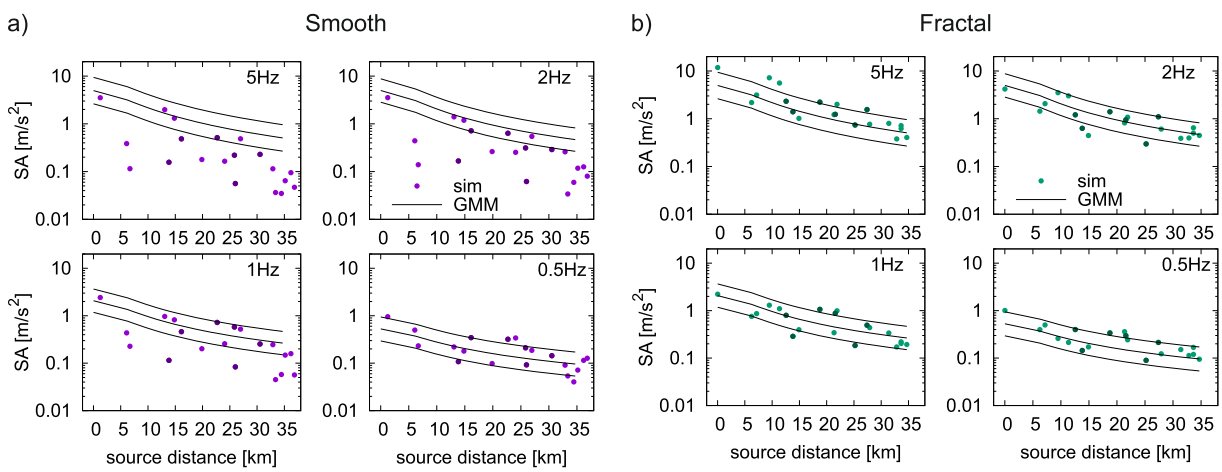

Figure 11. Comparison of synthetic spectral acceleration (SA) ordinates at four selected frequencies with the ground motion model (GMM) of Central Italy by Sgobba et al. (2021), for the (a) smooth and (b) fractal distributions of dynamic parameters for the Amatrice earthquake of Figure 7 at 20 stations. Stations with weak site effects from Figure 6 are shown by darker color. Note especially the improvement of SAs at 5 Hz for the small-scale fractal rupture. Moreover, above 1 Hz the complex rupture propagation of the fractal model also decreases the within-event variability due to the weakened directivity effect.

21699356, 2023, 6, Downloaded from https://agupubs.onlinelibrary.wiley.com/doi/10.1029/2023JB026506 by Charles University, Wiley Online Library on [15/01/2024]. See the Terms and Conditions (https://onlinelibrary.wiley.com/terms-and-conditions) on Wiley Online Library for rules of use; OA articles are governed by the applicable Creative Commons License

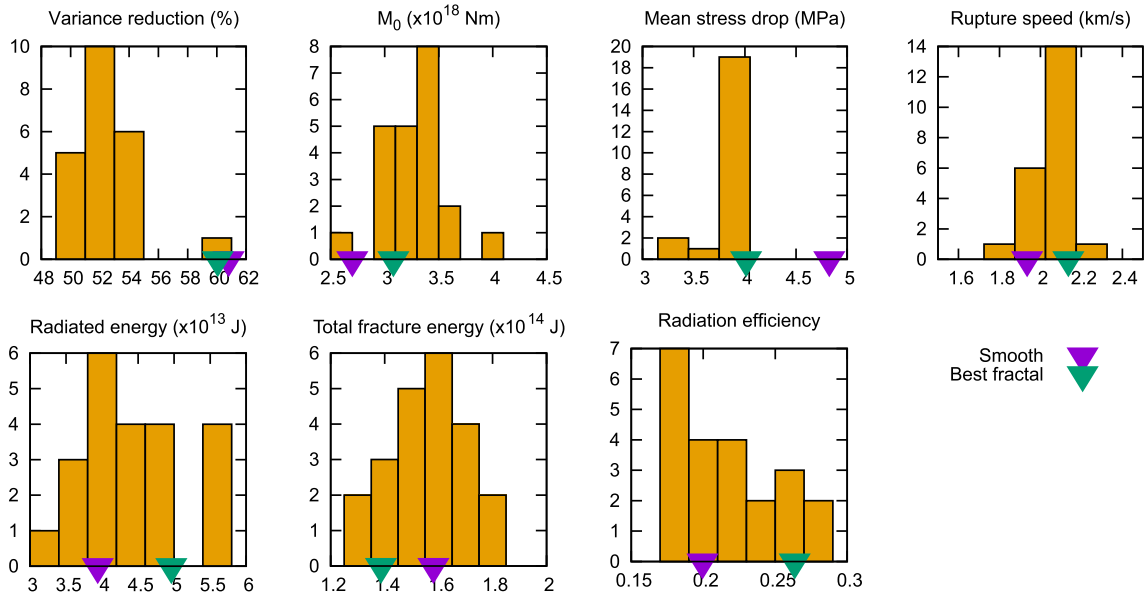

Figure 12. Gross parameters of the fractal rupture models of the Amatrice earthquake with random realizations of the small-scale dynamic rupture properties. All models have variance reduction of the low-frequency waveforms (<0.5 Hz) larger than 0.5. Parameters of the original (unperturbed) smooth model and the fractal model with the best fit with low-frequency seismograms are shown by triangles (see legend). We note that the parameters agree well although the models with smooth and highly variable dynamic rupture properties are compared.

larger G_c as the earthquake size (magnitude) increases. Note that there are other explanations of the G_c scaling, for example, thermal weakening (Lambert & Lapusta, 2020; Rice, 2006; Viesca & Garagash, 2015) or stress overshoot (Ke et al., 2022). Nevertheless, one can expect a mixture of such effects in nature, suggesting that D_c indeed is to be considered a proxy parameter.

Contrarily, there does not seem to be any empirical size dependence of the stress drop (or prestress) and strength of faults. Therefore, Ide and Aochi (2005) considered constant values and proposed fractal perturbations solely for the slip-weakening distance. To test such a model, we recalculate the elliptical model of Figure 2, maintaining the variations in D_c only. We thus introduce the perturbations to fracture energy G_c while keeping the S-parameter constant. To alleviate the increase of rupture speed due to smaller fracture energy with respect to the model of Figure 2, parameter c_D of Equation 9 controlling the amplitude of D_c is set to 2 in this simulation. Figure 13 shows selected dynamic and kinematic parameters, their cross-sections, and moment rate function. The latter exhibits an omega-square spectral shape, but the moment jerk lacks high-frequency peaks at later times. The slip distribution is relatively smooth, as in the previous case, while the stress drop is smoother. The peak slip rates attain lower amplitudes than in the case of including the variations in prestress and strength. The rupture velocity is heterogeneous only at the beginning of the rupture propagation, becoming gradually more homogeneous. Moreover, the rupture becomes supershear over a large area in the in-plane direction above the nucleation patch (Figure 13). This behavior was also observed by Renou et al. (2022), suggesting that the macroscopic rupture is controlled predominantly by the large D_c values in the later stage. We propose that without the variations in prestress and strength (and thus in the S-parameter), the rupture surpasses the small-scale heterogeneities after the energy release rate becomes sufficiently large, decreasing variations of the rupture velocity.

The average fracture energy of this model is 31 MJ/m^2, higher than 22 MJ/m^2 of the smooth model. Contrarily, the fractal model with perturbations in all 3 parameters has fracture energy 20 MJ/m^2, much closer to the original model. The proposed variations of initial stress and strength are limited and locally depend on D_c in such a way that smaller patches are more prone to failure (have a smaller value of the S-parameter) due to smaller strength and larger prestress, in addition to their smaller D_c (see Figure 1b). It can be interpreted as follows: the small patches of small D_c (and thus small G_c) correspond to more planar areas better aligned with the macroscopic fault plane and regional stress so that they are closer to failure and easier to break. Our numerical observations can be scrutinized by a rigorous mathematical analysis using homogenization techniques in future work (Barras et al., 2017; Latour et al., 2011).

21699356, 2023, 6, Downloaded from https://agupubs.onlinelibrary.wiley.com/doi/10.1029/2023JB026506 by Charles University, Wiley Online Library on [15/01/2024]. See the Terms and Conditions (https://onlinelibrary.wiley.com/terms-and-conditions) on Wiley Online Library for rules of use; OA articles are governed by the applicable Creative Commons License

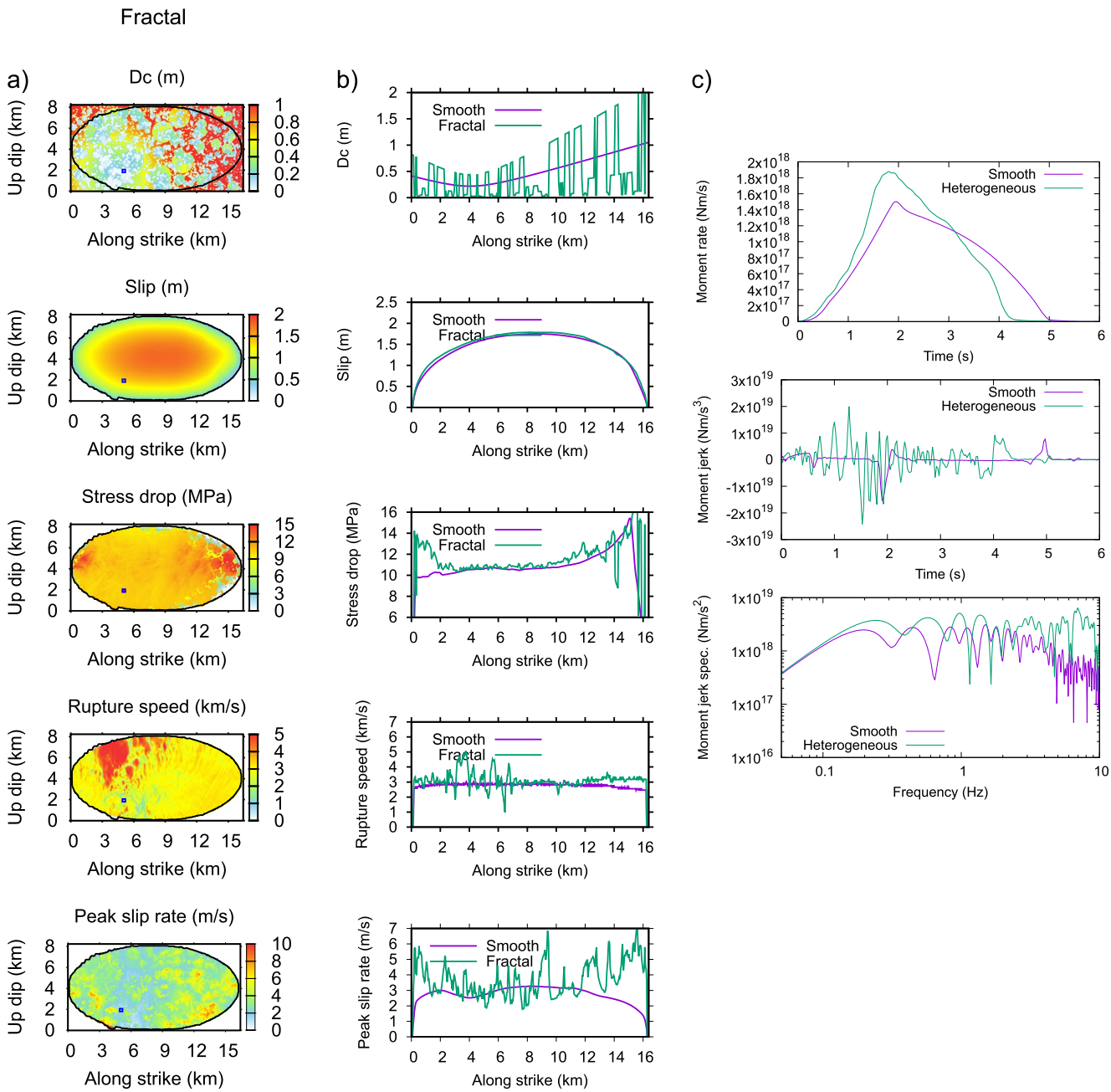

Figure 13. Dynamic and kinematic rupture parameters of the elliptical model if only variations in slip-weakening distance D_c are considered. (a) Along-fault distribution of the parameters (see legend) and (b) cross-sections of the respective parameters through the middle of the fault (see legend). To alleviate the increase of rupture speed due to smaller fracture energy with respect to the model of Figure 2, parameter c_D of Equation 9 controlling the amplitude of D_c is set to 2 in this simulation. Note the systematic, almost homogeneous supershear rupture propagation in the in-plane (up-dip) direction, and the decaying variations of the rupture velocity in the anti-plane (along-strike) direction as the rupture front becomes almost insensitive to the small-scale perturbations in D_c. (c) Moment rate functions, their second-time derivatives (jerks), and moment jerk spectra corresponding to the model with smooth parameters and with fractal small-scale perturbations in D_c only. Note the high-frequency jerks of the latter model decay with time although its spectrum still has omega-squared shape (i.e., plateau).

Although the scaling property of the model might suggest the possibility of explaining the Gutenberg-Richter relation, we do not aim to interpret it here further, mainly because most aftershocks likely occur off the main fault. Its essence is to introduce the small-scale radiation of a single earthquake effectively and not to describe the whole earthquake cycle, where many more effects are at play. In particular, the variations in stress would not depend only on the scale of the patches but also on the faulting history. We admit that if our systematic behavior

21699356, 2023, 6, Downloaded from https://agupubs.onlinelibrary.wiley.com/doi/10.1029/2023JB026506 by Charles University, Wiley Online Library on [15/01/2024]. See the Terms and Conditions (https://onlinelibrary.wiley.com/terms-and-conditions) on Wiley Online Library for rules of use; OA articles are governed by the applicable Creative Commons License

21699356, 2023, 6, Downloaded from https://agupubs.onlinelibrary.wiley.com/doi/10.1029/2023JB026506 by Charles University, Wiley Online Library on [15/01/2024]. See the Terms and Conditions (https://onlinelibrary.wiley.com/terms-and-conditions) on Wiley Online Library for rules of use; OA articles are governed by the applicable Creative Commons License

of the initial stress being smaller for larger patches (events) was valid, it would imply a decrease of stress drop with increasing magnitude, contradicting constant stress-drop scaling (Kanamori & Brodsky, 2004).

The important choices of parameters for the fractal template that was found thanks to extensive numerical testing are the background distribution parameters r_0 and N_0 (see Equations 7 and 8) used in Equations 5 and 6, respectively. Considering that for larger earthquakes, $\min(L,W) = W$ (i.e., faults are relatively longer than wider) and $W \sim$ 15–20 km (corresponding to the seismogenic depth), we find r_0 = 2–2.5 km, which corresponds to S-wave wavelengths at frequencies of 0.6–1 Hz. We remind the reader that these values agree with the standard threshold frequency between deterministic and stochastic earthquake source modeling (Ameri et al., 2012; Gallovič, 2016; Graves & Pitarka, 2016). N_0 is then defined to reconcile the number of patches for larger aspect ratios. Although it was not thoroughly tested, we suppose that the parameters specified in this study can be utilized in general.

4.3. Relation Between Gross Parameters of the Smooth and Fractal Models

Dynamic source inversions generally employ only the low-frequency part of seismic waveforms mainly due to limitations in the velocity models considered in wave propagation modeling. Therefore, inferred models are smooth despite the anticipated heterogeneity of the true faulting parameters. The relation between the low-frequency smooth dynamic models and the true ones is an obvious yet open question.

In this study, we address this problem by comparing selected parameters of the original low-frequency model with its fractal counterparts for the Amatrice earthquake (Figure 12). There is a general agreement between the respective quantities, perhaps except for the average stress drop that is lower for the fractal model. As we explain in the text, the latter can be leveraged and fine-tuned by adjusting the parameters of the fractal perturbations. Nonetheless, the general agreement of the gross parameters suggests that the main features inferred by dynamic source inversions (fracture energy, radiation efficiency, etc.) can be considered representative despite being constrained by low-frequency data only, neglecting small-scale source variations.

4.4. Rupture Nucleation in the Fractal Model

Rupture nucleation is a well-known problem in dynamic rupture simulations because it can significantly impact the rupture propagation and dominate the early part of the seismograms, unlike what is observed empirically (Galis et al., 2015). To avoid such artifacts, we considered nucleation from a small patch of low D_c in both the smooth and fractal elliptical models. The rupture then progressively propagates to areas of large D_c, following the original idea of Ide and Aochi (2005).

In the second example of the Amatrice dynamic model, the fractal perturbations applied to the smooth model affect the nucleation area, too. In particular, the nucleation in the fractal model is weakened due to the decrease of the nucleation overstress, even below its critical size (Galis et al., 2015). In such cases, the rupture could grow beyond the nucleation only in favorable circumstances when sufficiently small patches of low D_c (and thus G_c) are distributed in the vicinity of the nucleation patch, promoting the rupture evolution. This explains why some of the tested realizations of the fractal perturbations did not rupture the fault and thus underpredicted the seismic moment.

5. Conclusions

We have presented and tested an approach to enrich initially smooth dynamic rupture models on a planar fault by small-scale random fractal variations in fracture energy and prestress (S-parameter). Assuming the slip-weakening friction law, we perturb slip-weakening distance, initial stress, and strength. We demonstrate that the small-scale fractal properties can only mildly affect the large-scale rupture evolution, thereby introducing the perturbations in a robust way. The method is presented using an ad-hoc elliptical dynamic rupture model. It is also shown to improve the fit of the 2016 M_w 6.2 Amatrice earthquake recordings in the frequency range of 0–10 Hz and to match the Central Italy GMM of Sgobba et al. (2021) in terms of SAs up to 5 Hz.

The presented fractal perturbations alleviate many issues of simple dynamic rupture models with smooth properties or only fractal initial stress. Our small-scale fractal variations in all dynamic parameters (substituting rough fault features while permitting simulations on planar faults) result in sustained high-frequency radiation

21699356, 2023, 6, Downloaded from https://agupubs.onlinelibrary.wiley.com/doi/10.1029/2023JB026506 by Charles University, Wiley Online Library on [15/01/2024]. See the Terms and Conditions (https://onlinelibrary.wiley.com/terms-and-conditions) on Wiley Online Library for rules of use; OA articles are governed by the applicable Creative Commons License

during the rupture propagation, mainly due to the random heterogeneous acceleration and deceleration of the rupture front. The slip rates are complex on short scales, resembling delayed or advanced rupturing of overlapping patches in random directions, decreasing the directivity effect at high frequencies. The source time function and ASTF follow an omega-square spectral model. The nucleation of the event can initiate from a small patch with a short characteristic slip-weakening distance, hierarchically continuing the growth, resulting in a weak onset of the seismograms as in real recordings. These features, together with the simple incorporation in any dynamic planar model and the possibility to combine it with complex 3D Green's functions, make the proposed approach a promising choice for strong-motion simulations in a broad frequency range of engineering interests.

Data Availability Statement

All seismic data and metadata related to the Amatrice earthquake and accelerometric stations used in this study were downloaded from the Engineering Strong-Motion (ESM) database (https://esm-db.eu/; Lanzano et al., 2021). All simulations were performed using code FD3D_TSN by Premus et al. (2020), available at GitHub (https://github.com/JanPremus/fd3d_TSN).

Acknowledgments
We thank the Associate Editor, Ruth Harris, and an anonymous reviewer for their valuable feedback that helped improve our manuscript. We acknowledge financial support from the Czech Science Foundation (project 23-06345S).

References

Abercrombie, R. E., & Rice, J. R. (2005). Can observations of earthquake scaling constrain slip weakening? *Geophysical Journal International*, *162*(2), 406–424. https://doi.org/10.1111/j.1365-246x.2005.02579.x

Adda-Bedia, M., & Madariaga, R. (2008). Seismic radiation from a kink on an anti-plane fault. *Bulletin of the Seismological Society of America*, *98*(5), 2291–2302. https://doi.org/10.1785/0120080003

Akinci, A., Aochi, H., Herrero, A., Pischiutta, M., & Karanikas, D. (2017). Physics-based broadband ground-motion simulations for probable $M_w \geq 7.0$ earthquakes in the Marmara Sea region (Turkey). *Bulletin of the Seismological Society of America*, *107*(3), 1307–1323. https://doi.org/10.1785/0120160096

Ameri, G., Gallovič, F., & Pacor, F. (2012). Complexity of the M_w 6.3 2009 L'Aquila (Central Italy) earthquake: 2. Broadband strong motion modeling. *Journal of Geophysical Research: Solid Earth*, *117*(B4), B04308. https://doi.org/10.1029/2011jb008729

Andrews, D. J. (1976). Rupture velocity of plane strain shear cracks. *Journal of Geophysical Research*, *81*(32), 5679–5687. https://doi.org/10.1029/jb081i032p05679

Andrews, D. J., & Ma, S. (2016). Validating a dynamic earthquake model to produce realistic ground motion. *Bulletin of the Seismological Society of America*, *106*(2), 665–672. https://doi.org/10.1785/0120150251

Aochi, H., & Ide, S. (2004). Numerical study on multi-scaling earthquake rupture. *Geophysical Research Letters*, *31*, L02606. https://doi.org/10.1029/2003GL018708

Aochi, H., & Ide, S. (2014). Ground motions characterized by a multi-scale heterogeneous earthquake model. *Earth Planets and Space*, *66*(1), 42. https://doi.org/10.1186/1880-5981-66-42

Aochi, H., & Twardzik, C. (2020). Imaging of seismogenic asperities of the 2016 ML 6.0 Amatrice, Central Italy, earthquake through dynamic rupture simulations. *Pure and Applied Geophysics*, *177*(5), 1931–1946. https://doi.org/10.1007/s00024-019-02199-z

Aochi, H., & Ulrich, T. (2015). A probable earthquake scenario near Istanbul determined from dynamic simulations. *Bulletin of the Seismological Society of America*, *105*(3), 1468–1475. https://doi.org/10.1785/0120140283

Barras, F., Geubelle, P. H., & Molinari, J.-F. (2017). Interplay between process zone and material heterogeneities for dynamic cracks. *Physical Review Letters*, *119*(14), 144101. https://doi.org/10.1103/physrevlett.119.144101

Baumann, C., & Dalguer, L. A. (2014). Evaluating the compatibility of dynamic rupture-based synthetic ground motion with empirical ground-motion prediction equation. *Bulletin of the Seismological Society of America*, *104*(2), 634–652. https://doi.org/10.1785/0120130077

Beeler, N. M. (2023). On the scale-dependence of fault surface roughness. *Journal of Geophysical Research: Solid Earth*, *128*(2), e2022JB024856. https://doi.org/10.1029/2022jb024856

Berenger, J.-P. (1994). A perfectly matched layer for the absorption of electromagnetic waves. *Journal of Computational Physics*, *114*(2), 185–200. https://doi.org/10.1006/jcph.1994.1159

Bernard, P., Herrero, A., & Berge, C. (1996). Modeling directivity of heterogeneous earthquake ruptures. *Bulletin of the Seismological Society of America*, *86*, 1149–1160.

Boatwright, J. (1988). The seismic radiation from composite models of faulting. *Bulletin of the Seismological Society of America*, *78*, 489–508.

Boore, D. M., Stewart, J. P., Seyhan, E., & Atkinson, G. M. (2014). NGA-West2 equations for predicting PGA, PGV, and 5% damped PSA for shallow crustal earthquakes. *Earthquake Spectra*, *30*(3), 1057–1085. https://doi.org/10.1193/070113eqs184m

Bruhat, L., Fang, Z., & Dunham, E. M. (2016). Rupture complexity and the supershear transition on rough faults. *Journal of Geophysical Research: Solid Earth*, *121*(1), 210–224. https://doi.org/10.1002/2015jb012512

Chiaraluce, L., Di Stefano, R., Tinti, E., Scognamiglio, L., Michele, M., Casarotti, E., et al. (2017). The 2016 Central Italy seismic sequence: A first look at the mainshocks, aftershocks, and source models. *Seismological Research Letters*, *88*(3), 757–771. https://doi.org/10.1785/0220160221

Cirella, A., Pezzo, G., & Piatanesi, A. (2018). Rupture kinematics and structural-rheological control of the 2016 M_w 6.1 Amatrice (Central Italy) earthquake from joint inversion of seismic and geodetic data. *Geophysical Research Letters*, *45*(22), 12302–12311. https://doi.org/10.1029/2018gl080894

Cotton, F., & Coutant, O. (1997). Dynamic stress variations due to shear faults in a plane-layered medium. *Geophysical Journal International*, *128*(3), 676–688. https://doi.org/10.1111/j.1365-246x.1997.tb05328.x

Dalguer, L. A., & Day, S. M. (2007). Staggered-grid split-node method for spontaneous rupture simulation. *Journal of Geophysical Research*, *112*(B2), B02302. https://doi.org/10.1029/2006jb004467

Das, S., & Aki, K. (1977). A numerical study of two-dimensional spontaneous rupture propagation. *Geophysical Journal International*, *50*(3), 643–668. https://doi.org/10.1111/j.1365-246x.1977.tb01339.x

Day, S. M. (1982). Three-dimensional simulation of spontaneous rupture: The effect of nonuniform prestress. *Bulletin of the Seismological Society of America*, *72*, 1881–1902.
Dunham, E. M., Belanger, D., Cong, L., & Kozdon, J. E. (2011). Earthquake ruptures with strongly rate-weakening friction and off-fault plasticity, Part 2: Nonplanar faults. *Bulletin of the Seismological Society of America*, *101*(5), 2308–2322. https://doi.org/10.1785/0120100076
Frankel, A. (1991). High-frequency spectral falloff of earthquakes, fractal dimension of complex rupture, b value, and the scaling of strength on faults. *Journal of Geophysical Research*, *96*(B4), 6291–6302. https://doi.org/10.1029/91jb00237
Fukuyama, E., & Mikumo, T. (1993). Dynamic rupture analysis: Inversion for the source process of the 1990 Izu-Oshima, Japan, earthquake. *Journal of Geophysical Research*, *98*(B4), 6529–6542. https://doi.org/10.1029/92jb02451
Galis, M., Pelties, C., Kristek, J., Moczo, P., Ampuero, J.-P., & Mai, P. M. (2015). On the initiation of sustained slip-weakening ruptures by localized stresses. *Geophysical Journal International*, *200*(2), 890–909. https://doi.org/10.1093/gji/ggu436
Gallovič, F. (2016). Modeling velocity recordings of the M_w 6.0 South Napa, California, earthquake: Unilateral event with weak high-frequency directivity. *Seismological Research Letters*, *87*(1), 2–14. https://doi.org/10.1785/0220150042
Gallovič, F., & Burjánek, J. (2007). High-frequency directivity in strong ground motion modeling methods. *Ann. Geophys.*, *50*, 203–211.
Gallovič, F., & Valentová, Ľ. (2020). Earthquake stress drops from dynamic rupture simulations constrained by observed ground motions. *Geophysical Research Letters*, *47*(4), e2019GL085880. https://doi.org/10.1029/2019gl085880
Gallovič, F., Valentová, L., Ampuero, J.-P., & Gabriel, A.-A. (2019a). Bayesian dynamic finite-fault inversion: 1. Method and synthetic test. *Journal of Geophysical Research: Solid Earth*, *124*(7), 6949–6969. https://doi.org/10.1029/2019jb017510
Gallovič, F., Valentová, L., Ampuero, J.-P., & Gabriel, A.-A. (2019b). Bayesian dynamic finite-fault inversion: 2. Application to the 2016 M_w 6.2 Amatrice, Italy, earthquake. *Journal of Geophysical Research: Solid Earth*, *124*(7), 6970–6988. https://doi.org/10.1029/2019jb017512
Gallovič, F., Zahradník, J., Plicka, V., Sokos, E., Evangelidis, C., Fountoulakis, I., & Turhan, F. (2020). Complex rupture dynamics on an immature fault during the 2020 M_w 6.8 Elazığ earthquake, Turkey. *Communications Earth & Environment*, *1*, 40. https://doi.org/10.1038/s43247-020-00038-x
Galvez, P., Petukhin, A., Somerville, P., Ampuero, J.-P., Miyakoshi, K., Peter, D., & Irikura, K. (2021). Multicycle simulation of strike-slip earthquake rupture for use in near-source ground-motion simulations. *Bulletin of the Seismological Society of America*, *111*(5), 2463–2485. https://doi.org/10.1785/0120210104
Graves, R. W. (1996). Simulating seismic wave propagation in 3D elastic media using staggered-grid finite differences. *Bulletin of the Seismological Society of America*, *86*, 1091–1106.
Graves, R. W., & Pitarka, A. (2010). Broadband ground-motion simulation using a hybrid approach. *Bulletin of the Seismological Society of America*, *100*(5A), 2095–2123. https://doi.org/10.1785/0120100057
Graves, R. W., & Pitarka, A. (2016). Kinematic ground motion simulations on rough faults including effects of 3D stochastic velocity perturbations. *Bulletin of the Seismological Society of America*, *106*(5), 2136–2153. https://doi.org/10.1785/0120160088
Guatteri, M., Mai, P. M., & Beroza, G. C. (2004). A pseudo-dynamic approximation to dynamic rupture models for strong ground motion prediction. *Bulletin of the Seismological Society of America*, *94*(6), 2051–2063. https://doi.org/10.1785/0120040037
Guatteri, M., & Spudich, P. (2000). What can strong-motion tell us about slip-weakening fault-friction law? *Bulletin of the Seismological Society of America*, *90*(1), 98–116. https://doi.org/10.1785/0119990053
Harris, R. A., Barall, M., Aagaard, B., Ma, S., Roten, D., Olsen, K., et al. (2018). A suite of exercises for verifying dynamic earthquake rupture codes. *Seismological Research Letters*, *89*(3), 1146–1162. https://doi.org/10.1785/0220170222
Harris, R. A., Barall, M., Lockner, D. A., Moore, D. E., Ponce, D. A., Graymer, R. W., et al. (2021). A geology and geodesy based model of dynamic earthquake rupture on the Rodgers Creek-Hayward-Calaveras fault system, California. *Journal of Geophysical Research: Solid Earth*, *126*(3), e2020JB020577. https://doi.org/10.1029/2020jb020577
Herrera, C., Ruiz, S., Madariaga, R., & Poli, P. (2017). Dynamic inversion of the 2015 Jujuy earthquake and similarity with other intraslab events. *Geophysical Journal International*, *209*(2), 866–875. https://doi.org/10.1093/gji/ggx056
Ide, S. (2019). Frequent observations of identical onsets of large and small earthquakes. *Nature*, *573*(7772), 112–116. https://doi.org/10.1038/s41586-019-1508-5
Ide, S., & Aochi, H. (2005). Earthquakes as multiscale dynamic ruptures with heterogeneous fracture surface energy. *Journal of Geophysical Research*, *110*(B11), B11303. https://doi.org/10.1029/2004jb003591
Ide, S., & Takeo, M. (1997). Determination of constitutive relations of fault slip based on seismic wave analysis. *Journal of Geophysical Research*, *102*(B12), 27379–27391. https://doi.org/10.1029/97jb02675
Irikura, K., & Miyake, H. (2011). Recipe for predicting strong ground motion from crustal earthquake scenarios. *Pure and Applied Geophysics*, *168*(1–2), 85–104. https://doi.org/10.1007/s00024-010-0150-9
Kanamori, H., & Brodsky, E. E. (2004). The physics of earthquakes. *Reports on Progress in Physics*, *67*(8), 1429–1496. https://doi.org/10.1088/0034-4885/67/8/r03
Kaneko, Y., & Shearer, P. M. (2015). Variability of seismic source spectra, estimated stress drop, and radiated energy, derived from cohesive-zone models of symmetrical and asymmetrical circular and elliptical ruptures. *Journal of Geophysical Research: Solid Earth*, *120*(2), 1053–1079. https://doi.org/10.1002/2014jb011642
Ke, C.-Y., McLaskey, G. C., & Kammer, D. S. (2022). Earthquake breakdown energy scaling despite constant fracture energy. *Nature Communications*, *13*(1), 1005. https://doi.org/10.1038/s41467-022-28647-4
Kheirdast, N., Ansari, A., & Custódio, S. (2021). Neuro-fuzzy kinematic finite-fault inversion: 2. Application to the M_w 6.2, August/24/2016, Amatrice earthquake. *Journal of Geophysical Research: Solid Earth*, *126*(8), e2020JB020773. https://doi.org/10.1029/2020jb020773
Kostka, F., Zahradník, J., Sokos, E., & Gallovič, F. (2022). Assessing the role of selected constraints in Bayesian dynamic source inversion: Application to the 2017 M_w 6.3 Lesvos earthquake. *Geophysical Journal International*, *228*(1), 711–727. https://doi.org/10.1093/gji/ggab359
Kristek, J., Moczo, P., & Galis, M. (2009). A brief summary of some PML formulations and discretizations for the velocity-stress equation of seismic motion. *Studia Geophysica et Geodaetica*, *53*(4), 459–474. https://doi.org/10.1007/s11200-009-0034-6
Lambert, V., & Lapusta, N. (2020). Rupture-dependent breakdown energy in fault models with thermo-hydro-mechanical processes. *Solid Earth*, *6*, 2283–2302. https://doi.org/10.5194/se-11-2283-2020
Lanzano, G., Felicetta, C., Pacor, F., Spallarossa, D., & Traversa, P. (2022). Generic-to-reference rock scaling factors for seismic ground motion in Italy. *Bulletin of the Seismological Society of America*, *112*(3), 1583–1606. https://doi.org/10.1785/0120210063
Lanzano, G., Luzi, L., Cauzzi, C., Bienkowski, J., Bindi, D., Clinton, J., et al. (2021). Accessing European strong-motion data: An update on ORFEUS coordinated services. *Seismological Research Letters*, *92*(3), 1642–1658. https://doi.org/10.1785/0220200398
Latour, S., Campillo, M., Voisin, C., Ionescu, I. R., Schmedes, J., & Lavallée, D. (2011). Effective friction law for small-scale fault heterogeneity in 3D dynamic rupture. *Journal of Geophysical Research*, *116*(B10), B10306. https://doi.org/10.1029/2010jb008118

21699356, 2023, 6, Downloaded from https://agupubs.onlinelibrary.wiley.com/doi/10.1029/2023JB026506 by Charles University, Wiley Online Library on [15/01/2024]. See the Terms and Conditions (https://onlinelibrary.wiley.com/terms-and-conditions) on Wiley Online Library for rules of use; OA articles are governed by the applicable Creative Commons License

Ma, S., Custodio, S., Archuleta, R., & Liu, P. (2008). Dynamic modeling of the 2004 M_w 6.0 Parkfield, California, earthquake. *Journal of Geophysical Research*, *113*(B2), B02301. https://doi.org/10.1029/2007jb005216

Madariaga, R. (1976). Dynamics of an expanding circular fault. *Bulletin of the Seismological Society of America*, *65*(3), 163–182. https://doi.org/10.1785/bssa0660030639

Madariaga, R. (1977). High-frequency radiation from crack (stress drop) models of earthquake faulting. *Geophysical Journal of the Royal Astronomical Society*, *51*(3), 625–651. https://doi.org/10.1111/j.1365-246x.1977.tb04211.x

Mai, P. M., Galis, M., Thingbaijam, K., Vyas, J., & Dunham, E. M. (2017). Accounting for fault roughness in pseudo-dynamic ground-motion simulations. *Pure and Applied Geophysics*, *174*(9), 3419–3450. https://doi.org/10.1007/s00024-017-1536-8

Mena, B., Dalguer, L. A., & Mai, P. M. (2012). Pseudodynamic source characterization for strike-slip faulting including stress heterogeneity and supershear ruptures. *Bulletin of the Seismological Society of America*, *102*(4), 1654–1680. https://doi.org/10.1785/0120110111

Mikumo, T., & Miyatake, T. (1978). Dynamical rupture process on a three-dimensional fault with non-uniform frictions and near-field seismic waves. *Geophysical Journal International*, *54*(2), 417–438. https://doi.org/10.1111/j.1365-246x.1978.tb04267.x

Mikumo, T., Olsen, K. B., Fukuyama, E., & Yagi, Y. (2003). Stress-break-down time and slip-weakening distance inferred from slip-velocity functions on earthquake faults. *Bulletin of the Seismological Society of America*, *93*(1), 264–282. https://doi.org/10.1785/0120020082

Miyamoto, T., Hirono, T., Yokoyama, Y., Kaneki, S., Yamamoto, Y., Ishikawa, T., et al. (2022). Characteristics of fault rocks within the aftershock cloud of the 2014 Orkney earthquake (M5.5) beneath the Moab Khotsong gold mine, South Africa. *Geophysical Research Letters*, *49*(14), e2022GL098745. https://doi.org/10.1029/2022gl098745

Ohnaka, M. (2003). A constitutive scaling law and a unified comprehension for frictional slip failure, shear fracture of intact rock, and earthquake rupture. *Journal of Geophysical Research*, *108*(B2), 2080. https://doi.org/10.1029/2000jb000123

Okuda, T., & Ide, S. (2018). Hierarchical rupture growth evidenced by the initial seismic waveforms. *Nature Communications*, *9*, 1–7. https://doi.org/10.1038/s41467-018-06168-3

Olsen, K. B., Day, S. M., Minster, J. B., Cui, Y., Chourasia, A., Okaya, D., et al. (2008). TeraShake2: Spontaneous rupture simulation of M_w 7.7 earthquakes on the Southern San Andreas fault. *Bulletin of the Seismological Society of America*, *98*(3), 1162–1185. https://doi.org/10.1785/0120070148

Olsen, K. B., Madariaga, R., & Archuleta, R. J. (1997). Three-dimensional dynamic simulation of the 1992 Landers earthquake. *Science*, *278*(5339), 834–838. https://doi.org/10.1126/science.278.5339.834

Olsen, K. B., & Mayhew, J. E. (2010). Goodness-of-fit criteria for broadband synthetic seismograms, with application to the 2008 M_w 5.4 Chino Hills, California, earthquake. *Seismological Research Letters*, *81*(5), 715–723. https://doi.org/10.1785/gssrl.81.5.715

Oral, E., Ampuero, J. P., Ruiz, J., & Asimaki, D. (2022). A method to generate initial fault stresses for physics-based ground-motion prediction consistent with regional seismicity. *Bulletin of the Seismological Society of America*, *112*(6), 2812–2827. https://doi.org/10.1785/0120220064

Pacor, F., Gallovič, F., Puglia, R., Luzi, L., & D'Amico, M. (2016). Diminishing high-frequency directivity due to a source effect: Empirical evidence from small earthquakes in the Abruzzo region, Italy. *Geophysical Research Letters*, *43*(10), 5000–5008. https://doi.org/10.1002/2016gl068546

Palmer, A., & Rice, J. (1973). The growth of slip surfaces in the progressive failure of over-consolidated clay. *Proceedings of the Royal Society of London A*, *332*, 527–548.

Peyrat, S., & Olsen, K. B. (2004). Nonlinear dynamic rupture inversion of the 2000 Western Tottori, Japan, earthquake. *Geophysical Research Letters*, *31*(5), L05604. https://doi.org/10.1029/2003gl019058

Pierantoni, P. P., Deiana, G., & Galdenzi, S. (2013). Stratigraphic and structural features of the Sibillini Mountains (Umbria-Marche Apennines, Italy). *Italian Journal of Geosciences*, *132*(3), 497–520. https://doi.org/10.3301/ijg.2013.08

Pischiutta, M., Akinci, A., Tinti, E., & Herrero, A. (2020). Broad-band ground-motion simulation of 2016 Amatrice earthquake, Central Italy. *Geophysical Journal International*, *224*(3), 1753–1779. https://doi.org/10.1093/gji/ggaa412

Pitarka, A., Graves, R., Irikura, K., Miyakoshi, K., Wu, C., Kawase, H., et al. (2022). Refinements to the Graves–Pitarka kinematic rupture generator, including a dynamically consistent slip-rate function, applied to the 2019 M_w 7.1 Ridgecrest earthquake. *Bulletin of the Seismological Society of America*, *112*, 287–306. https://doi.org/10.1785/0120210138

Pizzi, A., Di Domenica, A., Gallovič, F., Luzi, L., & Puglia, R. (2017). Fault segmentation as constraint to the occurrence of the main shocks of the 2016 Central Italy seismic sequence. *Tectonics*, *36*(11), 2370–2387. https://doi.org/10.1002/2017tc004652

Premus, J., Gallovič, F., Hanyk, L., & Gabriel, A. A. (2020). FD3D_TSN: A fast and simple code for dynamic rupture simulations with GPU acceleration. *Seismological Research Letters*, *91*(5), 2881–2889. https://doi.org/10.1785/0220190374

Pulido, N., & Dalguer, L. A. (2009). Estimation of the high-frequency radiation of the 2000 Tottori (Japan) earthquake based on a dynamic model of fault rupture: Application to the strong ground motion simulation. *Bulletin of the Seismological Society of America*, *99*(4), 2305–2322. https://doi.org/10.1785/0120080165

Ragon, T., Sladen, A., & Simons, M. (2019). Accounting for uncertain fault geometry in earthquake source inversions—II: Application to the M_w 6.2 Amatrice earthquake, Central Italy. *Geophysical Journal International*, *218*(1), 689–707. https://doi.org/10.1093/gji/ggz180

Renou, J., Vallée, M., & Aochi, H. (2022). Deciphering the origins of transient seismic moment accelerations by realistic dynamic rupture simulations. *Bulletin of the Seismological Society of America*, *112*(3), 1240–1251. https://doi.org/10.1785/0120210221

Renou, J., Vallée, M., & Dublanchet, P. (2019). How does seismic rupture accelerate? Observational insights from earthquake source time functions. *Journal of Geophysical Research*, *124*(8), 8942–8952. https://doi.org/10.1029/2019jb018045

Rice, J. R. (2006). Heating and weakening of faults during earthquake slip. *Journal of Geophysical Research*, *111*(B5), B05311. https://doi.org/10.1029/2005jb004006

Ripperger, J., Ampuero, J.-P., Mai, M. P., & Giardini, D. (2007). Earthquake source characteristics from dynamic rupture with constrained stochastic fault stress. *Journal of Geophysical Research*, *112*(B4), 1–17. https://doi.org/10.1029/2006jb004515

Ruiz, S., & Madariaga, R. (2013). Kinematic and dynamic inversion of the 2008 Northern Iwate earthquake. *Bulletin of the Seismological Society of America*, *103*(2A), 694–708. https://doi.org/10.1785/0120120056

Savran, W. H., & Olsen, K. B. (2020). Kinematic rupture generator based on 3-D spontaneous rupture simulations along geometrically rough faults. *Journal of Geophysical Research: Solid Earth*, *125*(10), e2020JB019464. https://doi.org/10.1029/2020jb019464

Schmedes, J., Archuleta, R. J., & Lavallée, D. (2013). A kinematic rupture model generator incorporating spatial interdependency of earthquake source parameters. *Geophysical Journal International*, *192*(3), 1116–1131. https://doi.org/10.1093/gji/ggs021

Scholz, C. (2002). *The mechanics of earthquake faulting*. Cambridge University Press.

Sgobba, S., Lanzano, G., & Pacor, F. (2021). Empirical nonergodic shaking scenarios based on spatial correlation models: An application to Central Italy. *Earthquake Engineering & Structural Dynamics*, *50*(1), 60–80. https://doi.org/10.1002/eqe.3362

Shi, Z., & Day, S. M. (2013). Rupture dynamics and ground motion from 3-D rough-fault simulations. *Journal of Geophysical Research*, *118*(3), 1122–1141. https://doi.org/10.1002/jgrb.50094

21699356, 2023, 6, Downloaded from https://agupubs.onlinelibrary.wiley.com/doi/10.1029/2023JB026506 by Charles University, Wiley Online Library on [15/01/2024]. See the Terms and Conditions (https://onlinelibrary.wiley.com/terms-and-conditions) on Wiley Online Library for rules of use; OA articles are governed by the applicable Creative Commons License

Song, S. G., Dalguer, L. A., & Mai, P. M. (2014). Pseudo-dynamic source modelling with 1-point and 2-point statistics of earthquake source parameters. *Geophysical Journal International*, *196*(3), 1770–1786. https://doi.org/10.1093/gji/ggt479

Taufiqurrahman, T., Gabriel, A.-A., Ulrich, T., Valentová, Ľ., & Gallovič, F. (2022). Broadband dynamic rupture modeling with fractal fault roughness, frictional heterogeneity, viscoelasticity and topography: The 2016 M_w 6.2 Amatrice, Italy earthquake. *Geophysical Research Letters*, *49*(22), e2022GL098872. https://doi.org/10.1029/2022gl098872

Tinti, E., Fukuyama, E., Piatanesi, A., & Cocco, M. (2005). A kinematic source-time function compatible with earthquake dynamics. *Bulletin of the Seismological Society of America*, *95*(4), 1211–1223. https://doi.org/10.1785/0120040177

Tinti, E., Scognamiglio, L., Michelini, A., & Cocco, M. (2016). Slip heterogeneity and directivity of the ML 6.0, 2016, Amatrice earthquake estimated with rapid finite-fault inversion. *Geophysical Research Letters*, *43*(20), 10745–10752. https://doi.org/10.1002/2016gl071263

Valentová, Ľ., Gallovič, F., & Hok, S. (2021). Near source ground motions and their variability derived from dynamic rupture simulations constrained by NGA-West2 GMPEs. *Bulletin of the Seismological Society of America*, *111*(5), 2559–2573. https://doi.org/10.1785/0120210073

Viesca, R. C., & Garagash, D. I. (2015). Ubiquitous weakening of faults due to thermal pressurization. *Nature Geoscience*, *8*(11), 875–879. https://doi.org/10.1038/ngeo2554

Withers, K. B., Olsen, K. B., Shi, Z., & Day, S. M. (2019). Validation of deterministic broadband ground motion and variability from dynamic rupture simulations of buried thrust earthquakes. *Bulletin of the Seismological Society of America*, *109*(1), 212–228. https://doi.org/10.1785/0120180005

Zeng, Y., Anderson, J., & Yu, G. (1994). A composite source model for computing realistic synthetic strong ground motions. *Geophysical Research Letters*, *21*(8), 725–728. https://doi.org/10.1029/94gl00367

21699356, 2023, 6, Downloaded from https://agupubs.onlinelibrary.wiley.com/doi/10.1029/2023JB026506 by Charles University, Wiley Online Library on [15/01/2024]. See the Terms and Conditions (https://onlinelibrary.wiley.com/terms-and-conditions) on Wiley Online Library for rules of use; OA articles are governed by the applicable Creative Commons License